Caveolin-1 regulates context-dependent signaling and survival in Ewing Sarcoma.

Dagan Segal[1], Xiaoyu Wang[2], Hanieh Mazloom-Farisbaf[1], Divya Rajendran[1], Erin Butler[3,4], Bingying Chen[1], Bo-Jui Chang[1], Khushi Ahuja[1], Averi Perny[1], Kushal Bhatt[1], Dana Kim Reed[1], Diego H. Castrillon[5], Jeon Lee[1], Elise Jeffery[6], Lei Wang[1,7], Noelle S. Williams[2], Stephen X. Skapek[3,4], Satwik Rajaram[1], Reto Fiolka[1,7], Gary Hon[1,8], James F. Amatruda[9,10*], Gaudenz Danuser[1*]

1. *Lyda Hill Department of Bioinformatics, UT Southwestern Medical Center, Dallas, TX*
2. *Department of Biochemistry, UT Southwestern Medical Center, Dallas, TX*
3. *Department of Pediatrics, Division of Hematology/Oncology, University of Texas Southwestern Medical Center, Dallas, TX, USA.*
4. *Harold C. Simmons Comprehensive Cancer Center, University of Texas Southwestern Medical Center, Dallas, TX, USA.*
5. *Department of Pathology, UT Southwestern Medical Center, Dallas, TX*
6. *Children's Medical Center Research Institute, UT Southwestern Medical Center, Dallas, TX*
7. *Department of Cell Biology, UT Southwestern Medical Center, Dallas, TX*
8. *Green Center for Reproductive Biological Sciences, UT Southwestern Medical Center, Dallas, TX*
9. *Department of Pathology and Laboratory Medicine, Children's Hospital Los Angeles, Keck School of Medicine, University of Southern California, Los Angeles, CA*
10. *Cancer and Blood Disease Institute, Children's Hospital Los Angeles; Keck School of Medicine, University of Southern California, Los Angeles, CA*

**co-corresponding authors*

ABSTRACT:

Cellular plasticity is a hallmark function of cancer, but many of the underlying mechanisms are not well understood. We uncover Caveolin-1, a scaffolding protein that modulates plasma membrane domain organization, as a context-specific regulator of survival signaling in Ewing sarcoma (EwS). Single cell analysis reveals a distinct subpopulation of EwS cells, which highly express the cell surface marker CD99 as well as Caveolin-1. *CD99 High* cells isolated through flow cytometry differ from *CD99 Low* cells in morphology, gene expression, and survival capabilities *in vivo.* Our work demonstrates that elevated Caveolin-1 expression in these cells plays a key role in the regulation of PI3K/AKT survival signaling, through subcellular organization of PI3K activity at the cell surface. We thus propose a model where the *CD99 High*

state develops a Cav-1 controlled signaling network to regulate cell survival that is distinct from the AKT-agnostic survival of *CD99 Low* cells. Overall, this work identifies a state transition of EwS cells and uncovers Caveolin-1 as a driver of survival signaling in a context-dependent manner.

INTRODUCTION

Cellular adaptation is a hallmark function of cancer, fueling intratumoral heterogeneity and contributing to tumor growth, metastasis, and therapeutic resistance [1]. Phenotypically distinct yet genetically similar subpopulations with different growth and metastatic capabilities have now been described across many cancer types and under varying stresses[2], but our understanding of the underlying mechanisms is still limited. The need to uncover non-genetic adaptation mechanisms is particularly apparent in pediatric cancers, which in many cases have low mutational burden beyond a single driver despite variability in patient outcome [3, 4]. In this work, we focus on Ewing sarcoma (EwS) as a prototype of pediatric cancer. EwS is the second most common malignant bone tumor occurring in children and young adults, characterized by a single chromosomal translocation leading to the formation of a chimeric fusion oncogene, most commonly EWS::FLI1 [5, 6]. While much research has focused on the oncogene EWS::FLI1 as the putative driver of distinct EwS cell states [7, 8], more recent works have identified EwS cell states with distinct gene signatures not classically associated with EWS::FLI1 gene expression [9-11] . In either case, the signaling mechanisms that drives segregation of cell states remains largely unknown.

One possible mechanism driving distinct cell states could be through regulation of signaling pathways on the plasma membrane, which integrates signals from the extracellular environment through targeted, localized signaling cascades. Specifically, differential organization of modified lipids [12] or activated receptors[13] on the cell surface into subcellular domains can affect downstream signaling. A prominent example of such domains can be observed in so-called caveolae, cave-like membrane invaginations that are rich in cholesterol and sphingolipids[14] and have roles in signal transduction [15-20]. Caveolae are prominently found in a subset of cell types, such as adipocytes and muscle cells, and have been implicated in many cancers[21, 22], including Ewing Sarcoma [23, 24]. Several studies have demonstrated that perturbation of these structures through mechanical means [25-27] or perturbations of the key structural protein Caveolin-1 affects major signaling pathways implicated in cancer, such as Src[16, 19, 20], Erk1/2[24, 28], and PI3K/Akt activation [29, 30]. Some of these studies have demonstrated differential subcellular organization of specific signaling molecules upon loss of caveolae [28, 31]. However, whether and how caveolae-

based organization of signal drives distinct functional cell states in development and disease remains unclear.

In this study, we discovered an EwS cell population enriched for an epithelial-to-mesenchymal gene signature that is characterized by high expression of the surface receptor CD99. *CD99 High* cells show decreased proliferation but higher viability compared to *CD99 Low* cells *in vivo* and in response to chemotherapeutic drugs. We find that *CD99 High* cells associate with high endogenous Caveolin-1 expression levels and show an enrichment for caveolae. Further experiments uncover Caveolin-1 dependent regulation of the PI3K/AKT signaling pathway, associated with cell survival, through subcellular organization of PI3K on the cell surface. Overall, this work identifies a mechanism for cell-autonomous, acute adaptation of survival signaling in a context-dependent manner.

RESULTS

High CD99 marks a distinct Ewing Sarcoma cell state.

Phenotypic heterogeneity is an inherent feature of cancer cells, and likely underlies disease progression and resistance to treatment [1]. To study heterogeneity in EwS cell populations, we first used single cell transcriptomics to identify cell surface markers that would readily enable isolation of distinct subpopulations for further downstream characterization (Figure 1A). Given that cell surface receptors are sensitive to cleavage through standard enzymatic passaging techniques and inspired by classic studies in mesenchymal stem cells [32-34], we reasoned that cells passaged through mechanical means rather than enzymatic cleavage could be used to enable the discovery of distinct subpopulations of cells, as well as preserve surface receptors intact as future targets for flow cytometry. We applied this approach to the EwS cell line TC71, and uncovered a cluster of cells with a unique transcriptional profile (Figure S1A), characterized by a distinct mesenchymal signature (Figure S1B). Interestingly, the differentially expressed genes showed little overlap with known EWSR1::FLI1 gene signatures (Figure S1C). While previous literature has associated the mesenchymal gene signature state with low EWSR1::FLI1 levels [8, 35-37], recent works have uncovered a distinct mesenchymal cell state driven by transcription factor ETV6[10, 11] that is distinct from the canonical EWSR1::FLI1 target gene signature. Consistent with this observation, ETV6 expression is decreased in the highlighted cluster, while the ETV6 target gene SOX11 is increased (Figure S1D), suggesting this population represents a differentiation program distinct from the “EWSR1::FLI1 low” cell state.

We next profiled cell surface proteins of the distinct cluster in TC71 cells, through relative expression of transcripts of surface receptors that could serve as flow cytometry targets[36]. Of the 348 targets examined, seven surface receptors were enriched (Figure 1D), with the glycoprotein receptor CD99 being among the most differentially expressed (Figure 1B,C). CD99 is a commonly used biomarker for EwS[38], making it a natural target for flow cytometry. To test the broader applicability of these findings, we also applied single-cell transcriptomics to cells isolated from two patient derived xenograft (PDX) lines, which have been passaged and subsequently extracted from subcutaneous xenografts in immunocompromised mice. These experiments also showed clusters with high CD99 expression and carried the mesenchymal gene signature (Figure 1D, S1B,E), suggesting CD99 could serve as a general marker for this particular cell state. To measure CD99 expression levels on the cell surface, we applied immunolabeling using a CD99-PE conjugated antibody to a single cell suspension of TC71 cells and measured relative fluorescence by flow cytometry. Consistent with the single-cell transcriptomics results, these experiments uncovered a bimodality of CD99 distributions, representing intermediate and high levels of CD99 protein expression (Fig 1E). Of note, the CD99 High state appears to be reversible, since TC71 *CD99 High* cells that were isolated and subsequently grown for several passages again displayed a bimodal distribution of CD99 expression upon flow cytometric analysis (Fig 1F).

CD99 High cells display differences in morphology, gene expression, and survival _in situ._

We next utilized CD99 as a cell sorting target, enabling isolation and further characterization of the distinct cell states. Following segregation by flow cytometry, differences in CD99 expression between *CD99 High* and *CD99 Low* cells were confirmed by western blot, while EWSR1::FLI1 protein expression levels remained consistent between the two groups (Fig S2A). Strikingly, the two subpopulations displayed distinct morphological phenotypes (Figure 2A, Figure S2A). The *CD99 High* cells were flat with thick actin bundles, while the *CD99 Low* cells appeared to be more rounded and in clusters, enriched for thin protrusions called filopodia. A morphologically distinct *CD99 High* population was also observed in RDES, another EwS cell line (Figure S2B). In addition, we observed that TC71 *CD99 High* cells displayed a marked enrichment of gene ontology terms related to neural differentiation by bulk transcriptomic analysis (Figure 2B). Functional growth and viability assays revealed no differences between *CD99 High* and *CD99 Low* cells when grown in adherent flasks (Fig S2C,D). However, *CD99 High* cells displayed decreased growth capabilities through *in vitro* assays in soft environments (Fig S2D).

To test whether *CD99 High* cells show distinct tumor growth or survival differences *in vivo,* we performed intratibial xenografts of isolated Luciferase-expressing *CD99 High* or *CD99 Low* TC71 cells, respectively, in immunocompromised mice. *CD99 High* cells showed dramatically lower tumor burden compared to *CD99 Low* cells (Figure 2C, S3A). A computed tomography scan also revealed that bony destruction, a phenomenon prototypic of EwS tumors described as moth-eaten appearance of the bone[28], was decreased in *CD99 High* cells (Figure 2D, S3B). Analysis of histological sections revealed that most tumor growth of *CD99 Low* cells occurs through the local invasion of surrounding muscle, while both cell populations grow masses of limited size within the medullary cavity of the bone (Figure 2E, S3C). To test for survival and growth differences between groups, we combined fluorescent staining of the apoptic marker TUNEL assay with immunostaining for the proliferation marker Ki67 to serially stained slides. For clusters of comparable size within the medullary cavity, the *CD99 Low* cells show comparable cell proliferation but strikingly more cell death compared to *CD99 High* cells (Figure 2F). Differences in cell death appear to hold true for local muscle invasions as well (Figure 2F, S3D). Of note, CD99 expression levels and cell morphologies appear to remain differential between the two populations *in situ,* as evidenced by immunohistochemistry (Figure S3C), and shape feature analysis (Figure S3E), respectively. Taken together, these results suggest that *CD99 High* cells represent a clinically distinct cell state, with potential survival advantage in certain microenvironments.

As an orthogonal approach to test distinctions in cell behavior in *CD99 High* cells, we performed cancer cell xenografts in the hindbrain ventricle (HBV) of 2-day old zebrafish. We first examined whether distinctions in cell state were maintained in this *in vivo* environment, using cell morphology as a functional readout of cell state, as previously described[39]. For this purpose, we injected a cell mixture consisting of 90% unsorted TC71 cells expressing the nuclear marker H2B-GFP, and 10% *CD99 High* or *CD99 Low* cells expressing the actin tag Ftractin-mRuby2 (Figure 3A-B). Following fixation in 4% paraformaldehyde (PFA) and 3D imaging of the zebrafish larvae at 1-day post-injection, we computationally extracted the cell volumes of individual *CD99 High* or *CD99 Low* cells for shape feature analysis to capture differences in cell morphotypes. This approach revealed a distinctly more protrusive, irregular cell shape in *CD99 High* cells (Figure 3C-D), suggesting that these cells maintain distinctions in their cell state *in vivo* in the zebrafish.

We next used xenografts in zebrafish to test differences in survival or proliferation between the two cell populations in the HBV. For this purpose, we first injected *CD99 High* or CD99 *Low*

cells expressing F-Tractin-mRuby2, respectively, into the HBV. Following chemical fixation at 2 days post-injection, we combined immunostaining of proliferation marker Phospho-histone-H3 (PH3) with TUNEL staining. Strikingly, *CD99 High* cells showed significantly less cell death and more proliferation than *CD99 Low* cells (Figure 3E-F). Taken together, these results suggest that the *CD99 High* population represents a transcriptionally and functionally distinct cell state, with survival advantages in certain tissues.

Caveolin-1 emerges as a potential driver of *CD99 High* State.

The discovery of a functionally distinct cell population in EwS cells led us to investigate potential drivers of the *CD99 High* state. Two initial lines of evidence converged around the protein Caveolin-1 (Cav-1) as a potential regulator of the EwS *CD99 High* cell state. First, Cav-1 expression was highly enriched at the transcript level in the TC71 *CD99 High* cluster by single-cell transcriptomics (Figure 4A). Second, through a functional proteomics screen based on a Reverse Phase Protein Array (RPPA), we observed Cav-1 as the most differentially enriched protein in the TC71 *CD99 High* cells compared to *CD99 Low* cells (Figure 4B). Protein measurement by western blot confirmed higher Cav-1 expression in *CD99 High* cells in TC71 and RDES cell lines (Figure 4C, S2B).

Cav-1 is the main structural protein responsible for cholesterol-rich membrane invaginations termed caveolae[14]. It is upregulated in metastases across several cancer types, including EwS, and has been implicated in diverse processes, including cell signaling, membrane trafficking, and stress response, making it a promising candidate for further investigation. To examine whether Cav-1-driven caveolae were enriched in *CD99 High* cells, we turned to ultrastructure analysis by electron microscopy. Indeed, we observed an abundance of caveolae in *CD99 High* cells but not in *CD99 low* cells (Figure 4C). Knockdown of Cav-1 in *CD99 High* cells abrogated the density of membrane invaginations, confirming that it is this shift in Cav-1 expression leading to the presence or absence of caveolae. (Figure 4C). As an orthogonal approach to measure the presence of caveolae, we examined the colocalization of endogenously tagged Cav-1-mClover with another marker of caveolae, termed PTRF/Cavin-1[40], through immunofluorescence. While Cav1-mClover colocalized strongly with PTRF in *CD99 High* cells, the *CD99 Low* cells showed decoupled PTRF and Caveolin-1 localization (Figure 4D-E). This is consistent with previous reports that Caveolin-1 can have both caveolar and non-caveolar localization patterns, with possibly distinct signaling functions [27, 31]. Analysis of timelapse

imaging shows distinctly smaller and less dynamic Cav-1 puncta in CD99-High cells (Figure S4B), another hallmark of stable caveolar structures.

To test whether Cav-1 drives the *CD99 High* state, we applied CD99-based flow cytometry to TC71 cells upon tetracycline (tet) -inducible knockdown of Cav-1, combined with an RFP reporter. As an internal control, we co-cultured the tet-inducible Cav-1 shRNA, RFP+ cells with naïve TC71 cells with no drug induced Cav-1 knockdown. The Cav1 shRNA expressing cells and naive cells could then be distinguished in flow cytometry by the presence or absence of the RFP reporter. Surprisingly, we observed not a decrease but an increase in *CD99 High* cells upon Cav-1 knockdown in TC71 cells (Figure S4C), with no change in the flat morphology or CD99 expression levels compared to naïve *CD99 High* cells, although formation of caveolae was lost, as observed by ultrastructure analysis (Figure 4C).

Despite the observation that knockdown of Cav-1 does not change the CD99 expression levels or morphology of *CD99 High* cells, we chose to test whether *CD99 High* cells display any Cav-1 dependent functional advantage. For this purpose, we co-cultured *CD99 High* and *CD99 Low* cells, with or without knockdown of Cav-1, respectively, and measured viability through flow cytometry (Figure 4F, S4D). We applied this assay with or without addition of the drug Doxorubicin (10uM), which is part of first-line therapy of EwS[38, 41]. Notably, Cav-1 knockdown did not confer an overall survival advantage in these experiments upon drug treatment (Figure S4D). However, closer examination of the surviving CD99+ cell population revealed a marked difference under drug treatment in CD99 distribution between the Cav-1 expressing and Cav-1 knockdown group (Figure 4G). The surviving cells with endogenous Cav-1 expression showed a prominent peak of *CD99 High* cells as measured by flow cytometry, suggesting the *CD99 High* cells have a survival advantage under these stress conditions. In contrast, cells with reduced Cav-1 expression appear to have lost the survival advantage of *CD99 High* cells, instead showing similar levels of *CD99 High* and *CD99 Low* peaks upon knockdown of Cav-1. Taken together, these results demonstrate that Cav-1 is required for the survival advantage of *CD99 High* cells under drug treatment, suggesting Cav-1 drives survival-based signaling in this cell state.

Caveolin-1 regulates PI3K/AKT signaling in *CD99 High* Cells

The change in viability upon drug treatment prompted us to examine changes in survival signaling pathways. By proteomics we noted in *CD99 High* cells an enrichment of Receptor Tyrosine Kinases (RTKs) that have been associated with the activation of the

phosphatidylinositol 3-kinase (PI3K)/AKT signaling pathway (Figure 4b, Table S1)[42-45]. Akt signaling is associated with cell growth, survival, and proliferation in cancer, and has been shown to be upregulated by Caveolin-1[29, 30]. Indeed, western blot showed increased AKT in its active form in *CD99 High* cells without induction of Cav-1 shRNA (Figure S5a). Knockdown of Caveolin-1 in TC71 cells drastically reduced phosphorylated AKT levels in *CD99 High* but not *CD99 Low* cells, suggesting only *CD99 High* cells depend on Caveolin-1 for their AKT signaling. However, by western blot the activation level of the upstream PI3K signal did not differ between the two cell states (Figure S5b). Notably, CD99 itself does not appear to be part of this pathway, since inducible knockdown of CD99 did not affect Cav-1 or phosphorylated AKT in *CD99 High* cells (Figure S5C).

PI3K signaling occurs specifically at the cell surface. It has previously been shown that downstream effects of PI3K signals on diverse cell functions depends on the spatial organization of the active molecule [46]. We therefore applied a high-resolution 3D imaging approach to measure the levels and organization of PI3K activity at the surfaces of individual TC71 cells. We employed a GFP-tagged AKT-PH construct as a reporter of the local concentration of PI3K-activated lipid products in *CD99 High* cells*, CD99 Low* cells*,* and *CD99 High* cells with Cav1 KD, embedded in 3D collagen (Figure 5A). To compare differences in overall intensity and signal organization between experimental groups, we leveraged Cellular Harmonics framework [47]. This method uses spectral decomposition of data on the cell surface to assess the spatial scales of signal organization in a cell-morphology-invariant manner. Using this approach, we detected no differences in overall enrichment of active PI3K between *CD99 High* and *CD99 Low* cells (Figure 5B), but major differences in the spatial organization of the signal (Figure 5A, 5C). Specifically, *CD99 High* cells displayed a more uniform distribution of active PI3K on the cell surface, with several hotspots across the entire cell. In contrast, *CD99 Low* cells displayed a more polarized or patchy distribution, with only a few hotspots detected in most cases. Upon Cav-1 knockdown, *CD99 High* cells displayed higher overall enrichment of active PI3K on the cell surface (Figure 5B), but a strikingly more polarized distribution compared to *CD99 High* cells (Figure 5C). Taken together, these results suggest that the uniform distribution of active PI3K in *CD99 High* cells promotes a more effective signal transduction to AKT and downstream survival in a Cav-1 dependent manner.

We hypothesized that differences in PI3K organization could be due to differences in fluidity of the cell membrane, which is modulated by caveolae[48]. Specifically, we expected that the high concentration of stable caveolae we had observed in *CD99 High* cells would reduce membrane

fluidity. To test the possibility of such a shift we used the mobility of the lipid nanodomain marker Cholera-toxin B-subunit (CTxB) as a proxy of internal membrane fluidity. Fluorescently tagged CTxB labels GM1 glycosphingolipid which allows tracking of lipid nanodomains by live-imaging [49]. Indeed, we observed an increase of GM1 dynamics in *CD99 High* cells upon Cav-1 knockdown (Figure 5D), indicating membrane nanodomain dynamics in *CD99 High* cells is Cav-1 dependent. Notably, labeling of GM1 in TC71 Cav1-mClover cells did not show co-localization of punctae (Figure S5D), indicating that the effect of caveolae on GM1 cluster mobility is indirect. Taken together, these results suggest that Cav-1 regulates PI3K organization through its effect on membrane dynamics on the cell surface.

DISCUSSION

In this study, we uncover a subpopulation of EwS cells characterized by distinctions in transcriptional signature, cell morphology, and growth *in vivo.* These cells can be identified and isolated through flow cytometry based on their high expression of the cell surface receptor CD99, a glycoprotein often used as a diagnostic marker in EwS[50]. Functional characterization demonstrates a survival advantage of *CD99 High* cells in certain tissues *in vivo* and in response to a chemotherapeutic drug. We identify the protein Cav-1 as a key regulator of this context-dependent cell survival in *CD99 High* cells, but not in *CD99 Low* cells, through regulation of PI3K signaling and membrane domains.

The acquisition of distinct cancer cell states drives drug resistance and metastasis in cancer [1], creating an urgent clinical need to better understand the underlying mechanisms. In EwS, as in many pediatric cancers[4], mutational tumor burden beyond a single driving mutation is low, suggesting non-genetic mechanisms are at play in modulating state heterogeneity. Several previous works have identified variability in expression levels of the oncogene EWS::FLI1 or its transcriptional signature as a driver of variable EwS cell states [8, 35-37], mostly through targeted knockdown of the oncogene and its targets. In contrast, the differences between *CD99 Low and CD99 High* cells described in this work appear to be agnostic to the oncogene level, but rather rely on Cav-1 as the modulator of cell state. Several recent studies have identified other potential drivers of EwS plasticity aside from EWS::FLI1. Some examples include depletion of the transcription co-factor ETV6, which drives a mesenchymal gene signature with upregulation of neural developmental genes[10, 11], or discovery of a cancer-associated fibroblast (CAF)-like tumor cell state identified by higher presence of the surface receptor CD73[9]. The *CD99 High* state could be comparable to both these cell states since it too exhibits mesenchymal and neural gene signatures, as well as low ETV6 expression and high expression of the neural

marker Sox11, compared to *CD99 Low* cells. While CD99 served as a useful marker of the distinct cell states, we did not find any evidence that CD99 itself is functionally significant in these cells. This contrasts with previous knockdown studies that showed that depletion of CD99 in EwS cells, rather than high CD99 levels, drives neural differentiation [50, 51].

Several studies have demonstrated that mechanical and biochemical cues, such as substrate detachment, matrix stiffness, and hypoxia affect activity of Cav-1[25-27], suggesting Cav-1 could potentially respond to cell-extrinsic cues to influence cell state. Cav-1 has also specifically been implicated in many cancers[21, 22], including EwS [23, 24]. We chose to pursue Cav-1 as a potential driver of distinct cell states in EwS cells due to the high expression levels of Cav-1 and striking difference in presence of Cav-1-driven caveolae in the *CD99 High* cells. Notably, Cav-1 knockdown did not affect cell morphology or CD99 expression levels. However, depletion of Cav-1 had striking effects on activation of downstream signaling pathways, and the ability of cells to survive under drug challenge. Since *CD99 Low* cells do not display caveolae, have different growth and survival phenotypes *in vitro* and *in situ*, and show distinct organization and expression of downstream signaling pathways, we presume this population of cells relies on alternative, Cav-1 independent mechanisms to regulate its cell state.

Cav-1 is known to regulate key cellular signaling pathways, such as Src- family kinases, receptor tyrosine kinases, and RAS signaling[16, 19, 20, 20, 29, 30]. Whether these effects are through direct binding of Cav-1 to components of the signaling pathway, or through alternate mechanisms, remains unclear. One possibility is that Cav-1 can indirectly influence downstream signaling by organizing lipids on the cell surface. This is evidenced by the protein's ability to selectively recruit specific lipids, such as cholesterol and PtdIns(4,5)P2, to caveolae [31], as well as its role in RAS nanoclustering[28]. Some studies have demonstrated flattening of caveolae and subsequent release of Cav-1 in response to mechanical stress[27, 52], suggesting that these structures can also serve as passive buffers of mechanical stress by acting as membrane reservoirs. Our work demonstrates Cav-1 dependent membrane nanodomain dynamics of the glycosphingolipid GM1, and Cav-1 dependent organization of active PI3K on the cell surface. These results lead us to a model whereby Cav-1 regulates PI3K organization in a specific subpopulation of EwS cells through its effect on membrane dynamics on the cell surface, driving context-dependent cell survival (Figure 5E). Specifically, *CD99 High* cells depend on high expression of Cav-1 and high caveolae density to organize the membrane through stabilization of lipid nanodomains such as GM1 and others. These make docking sites promiscuously available to PI3K localization, enhancing opportunities for stable signaling across the entire cell

surface. *CD99 Low* cells, or *CD99 High* cells with reduced Cav-1 expression, have dynamic, less stable nanodomains unable to widely spread PI3K's signaling power. Instead PI3K activity is localized to areas of high local curvature such as protrusions, as described in other works[53, 54]. Overall, these results describe a context-dependent signaling function of Cav-1 for regulation of distinct functional cell states in EwS. Future work will explore the cell extrinsic cues that drive Cav-1-dependent cell states in EwS, with the hopes of uncovering novel insights in EwS tumor biology that will guide treatment.

METHODS

Cell culture and cell line generation

Cells were cultured at 5% CO2 and 21% O2. TC71 and RDES cells were cultured using RPMI (Gibco) supplemented with 10% FBS and 1% antibiotic antimycotic. For mechanical passaging, cells were grown in T125 cell-culture treated flasks (Corning 430825), and iteratively washed with PBS by tapping of flask to detach cells. Cells were then reseeded in same flask for 2-6 weeks until mixed cell morphologies of the *CD99 High* and *CD99 Low* cell states were readily observed.

TC71 Cav1, EF1, and CD99 shRNA lines cells were generated using the pZIP shRNA Promoter selection kit (https://www.transomic.com/cms/home.aspx). shRNA knockdown was induced by continuous 1 µg/ml doxycycline in cell culture, and shRNA knockdown induction was verified RFP reporter expression and by Western blotting.

Fluorescent constructs were introduced into TC71 cells using the pLVX lentiviral system (Clontech) and selected using antibiotic resistance to either puromycin or neomycin. The GFP-FTractin and mRuby2-FTractin constructs contain residues 9–52 of the enzyme IPTKA30 fused to eGFP or mRuby2, respectively. pLenti6-H2B-GFP was acquired from Addgene (generated by Fuchs lab, New York University, plasmid # 25999; Addgene*).* The GFP-AktPH construct was obtained from the laboratory of Jason Haugh (North Carolina State University, Raleigh NC)[55] and cloned into the pLVX-IRES-puro vector (Clontech).

Endogenously tagged TC71 Cav-1-mClover was generated through CRISPR-based knock-in strategy. Briefly, two guides were generated using CRISPOR[56] (gRNA1: GCATCCCGATGGCACTCATC and gRNA2: GACCCACTCTTTGAAGCTGT), and were cloned into plasmid pSpCas9(BB)-2A-Puro (Feng Zhang lab, plasmid # 62988, Addgene). The donor

vector was generated using plasmid pMA-Tia1L which was a gift from Tilmann Bürckstümmer [57].

RPPA

Functional Proteomics Reverse Phase Protein Array (RPPA) was performed by RPPA core at MD Anderson Cancer Center. Cellular proteins were denatured in a 1% SDS + 2-mercaptoethanol buffer solution and diluted in five 2- fold serial dilutions in dilution lysis buffer. Serially diluted lysates were arrayed on nitrocellulose-coated slides (Grace Bio-Labs) by the Quanterix (Aushon) 2470 Arrayer (Quanterix Corporation). A total of 5808 spots were arrayed on each slide including spots corresponding to serially diluted (1) standard lysates, and (2) positive and negative controls prepared from mixed cell lysates or dilution buffer, respectively. Each slide was probed with a validated primary antibody plus a biotin-conjugated secondary antibody. Antibody validation for RPPA is described in the RPPA Core website: https://www.mdanderson.org/research/research-resources/core-facilities/functional-proteomics-rppacore/antibody-information-and-protocols.html. Signal detection was amplified using an Agilent GenPoint staining platform (Agilent Technologies) and visualized by DAB colorimetric reaction. The slides were scanned (Huron TissueScope, Huron Digital Pathology) and quantified using customized software (Array-Pro Analyzer, Media Cybernetics) to generate spot intensity. Relative protein level for each sample was determined by RPPA SPACE (developed by MD Anderson Department of Bioinformatics and Computational Biology, https://bioinformatics.mdanderson.org/public-software/rppaspace/)[58] by which each dilution curve was fitted with a logistic model. RPPA SPACE fits a single curve using all the samples (i.e., dilution series) on a slide with the signal intensity as the response variable and the dilution steps as the independent variable. The fitted curve is plotted with the signal intensities, both observed and fitted, on the y-axis and the log2 concentration of proteins on the x-axis for diagnostic purposes. The protein concentrations of each set of slides were then normalized for protein loading. Correction factor was calculated by (1) median-centering across samples of all antibody experiments; and (2) mediancentering across antibodies for each sample. Results were then normalized across RPPA sets by replicates-based normalization as described[59]. Details of the RPPA platform as performed by the RPPA Core are described in[60].

Transcriptomics

For single cell RNA-seq, RDES and TC71 cell lines were dissociated in Tryp-LE express enzyme (GIBCO), resuspended in 0.04% BSA in PBS, and passed through a 70um filter before diluting to 1000 cells/uL. NCH- EWS1 and SJEWS001321_X1 PDX lines were kindly provided by Peter Houghton (University of Texas Health Sciences center San Antonio), and St. Jude Childrens Research Hospital Childhood Solid Tumor Network (SJEWS001321_X1), respectively. For PDXs, tumor chunks >5 grams were dissociated using Trypsin and Collagenase, treated with a combination of DNAse and Magnesium Chloride to dissolve DNA, and passed through a 40um filter and treated with a Red Blood Cell lysis buffer before resuspending in 0.04% BSA in PBS and diluting to 1000 cells/uL. Samples were processed as in 10× Genomics Chromium 3' V3.1 with Cell Multiplexing kit and pooled together evenly for a final concentration of 1500 cells/μL in 0.04% BSA in PBS. Single-cell RNA-seq libraries were prepared using 10× Genomics Chromium 3′ V3.1 kit, following the standard protocol.

Single-cell RNA sequencing (scRNA-seq) data were generated for three samples: NCH-NCH-EWS1 PDX, SJEWS001321_X1 PDX, and TC71 cell line using the 10x Genomics platform. The data were processed using the Cell Ranger pipeline (version 6.0.0) to generate gene-barcode matrices, which were subsequently analyzed in Seurat (version 5.0.2). For each sample, raw count matrices, barcodes, and feature files were loaded into Seurat to create individual Seurat objects. Quality control was meticulously performed to exclude cells with extreme total RNA counts (nCount_RNA) and detected features (nFeature_RNA), with thresholds set based on the 5th and 95th percentiles for RNA counts, and the 10th and 90th percentiles for detected features. Additionally, cells with high mitochondrial content, indicative of potential cell stress or apoptosis, were filtered out by excluding cells with mitochondrial transcript percentages exceeding 15%. Data normalization was conducted using the "LogNormalize" method with a scale factor of 10,000, and highly variable features were identified using the "vst" method with 2,000 features selected for downstream analysis. Principal component analysis (PCA) was applied for dimensionality reduction, followed by clustering using the Louvain algorithm and visualization using Uniform Manifold Approximation and Projection (UMAP). Cell cycle scoring was performed by classifying cells into G1, S, and G2/M phases based on established markers. Specifically, cells in the G1 phase were subsetted for more focused analysis, ensuring that cell cycle effects were minimized in the downstream analyses. Gene Set Enrichment Analysis (GSEA) was conducted on the differentially expressed genes, utilizing pathways relevant to the EWSR1-FLI1 fusion as described by Siligan and Torchia. Furthermore, marker gene expression, such as CD99, was profiled across the different

clusters, and volcano plots were generated to highlight significant differentially expressed genes.

Flow Cytometry

For flow cytometry, TC71 cells were dissociated in Tryp-LE express enzyme, resuspended in 5% FBS in PBS, and passed through a 70um filter before diluting to 1X10^6 cells/mL. For live cell staining of CD99, cell suspension was incubated with mouse anti-human PE-CD99 antibody (BD Pharmingen 555689, 1:6). For shRNA expressing cell lines expressing RFP, cell suspension was incubated with rabbit monoclonal CD99 antibody (Abcam EPR3096 1:50) followed by secondary anti-rabbit antibody conjugated to AlexaFlour 405 (Abcam ab175652, 1:1000). For viability staining in Figure S4D, cells were additionally stained with 1:1000 Live-Dead fixable Far-Red stain (ThermoFisher L34973) prior to flow cytometry. Samples were anlayzed or sorted based on CD99 detected fluorophore intensity using BD FACSAria Zelda (BD BioSciences) flow cytometers. Flow cytometry plots were visualized using FloJo Software (BD Bioscences).

Western Blots

Primary antibodies used for western blotting were anti-CD99 (Abcam; EPR3096), Fli1 (Abcam; ab133485), Tubulin, Cav-1 (Cell Signaling; #3267), pAKT (Cell Signaling; #4060), AKT (Cell Signaling; #2920), Histone H3 (Cell Signaling: #9715), Phospho-PI3K (Invitrogen, #17387), PI3K (Cell Signaling, #42925).

Zebrafish husbandry and xenografts

Danio rerio were maintained in an Aquaneering aquatics facility according to industry standards. Vertebrate animal work was carried out by protocols approved by the institutional animal care and use committee at UT Southwestern, an Association for Assessment and Accreditation of Laboratory Animal Care accredited institution. Wild Indian Karyotype (WIK) wild-type lines used were obtained from the Zebrafish International Resource Center (zebrafish.org).

For xenografts of TC71-Ftractin-mRuby2 cells, cells were sorted for *CD99 High* and *CD99 Low* populations, then expanded prior to injection. Preparation of cell mixture consisted of 90% mRuby2-Ftractin labeled cells and 10% unsorted H2B-GFP labeled cells, or 100% mRuby2-Ftractin labeled cells, as indicated. Cell mixtures (2 × 106 cells) were run through a 70-µm cell strainer and resuspended in 5% FBS in PBS mixture for optimal cell viability.

Zebrafish embryos were collected, dechorionated, and treated with 0.1 mM phenylthiourea starting at 24 h post fertilization to prevent pigmentation. Xenografts were generated by microinjection of cell mixture into zebrafish larvae (2 d post fertilization [dpf]) with glass capillary needles into HBV. For each cell xenograft group, cells were injected into 3-aminobenzoic acid ethyl ester (Tricaine)–anesthetized embryos. Injected zebrafish larvae were incubated for 1–2 d in 34°C before imaging.

For immunostaining of zebrafish larvae, anesthetized embryos were fixed in 4% paraformaldehyde/1XPBS for 2 h in scintillation vials, rinsed in PBS +0.5% Tween, and stored in PBS up to 2 wk. Immunostaining was carried out as previously described (Miller et al., 2015). Primary antibodies were rabbit anti-GFP (ab290; Abcam) and mouse anti-Phospho-Histone H3 (9706S; Cell Signaling). TUNEL assay was performed using the ApopTag Green In-Situ Apoptosis Detection Kit (Millipore).

Mouse xenografts

All experiments involving animals were reviewed, approved, and monitored for compliance by the UT Southwestern Institutional Animal Care and Use Committee.

Lenti-luciferase-P2A-Neo was acquired from Addgene (Vakoc lab, Cold Spring Harbor Laboratory, plasmid: #105621; Addgene), and introduced into TC71 cells, which were subsequently sorted for *CD99 High and CD99 Low* populations and expanded prior to xenografts. Maintenance of isolated cell states was validated by distinct cell morphology in cell culture. Orthotopic intratibial xenografts were performed in NOD *scid* gamma chain knockout (NSG) mice, following a previously established protocol[61]. Briefly, the top of the right tibia was punctured with a 25 gauge needle, followed by injection of $5x10^5$ cells suspended in 5ul media into the medullar cavity of the bone using a 27 gauge needle from a tuberculine syringe (Cat 26040, Exelint, Int. Co, Redondo Beach, CA) coupled to a 0.1 ml Hamilton syringe (Cat 8001, Hamilton Co, Reno, NV).

Functional imaging to monitor tumor growth in live mice was performed using the IVIS Spectrum System (PerkinElmer). At each imaging session, 80 µL of a Luciferin working solution (40 mg/mL in PBS without calcium or magnesium) was administered. Mice were imaged at 0, 7, 14, 21, 28, 35, and 42 days post-injection. Regions of interest (ROIs) around the injection site were manually delineated for quantitative analysis of total flux [photons/second]. Luciferin signals

observed in the liver were excluded from the analysis. At the end of the experiment, tumor-bearing Grossly trimmed tibia samples and their encapsulating musculature and non-tumor bearing counter-parts from the same mouse were harvested for further evaluation.

For micro Computed Tomography (microCT) scans, formaline-fixed samples were scanned using a Scanco Medical µCT 35. Tibias were scanned at an isotropic voxel size of 3.5µm, with peak tube voltage of 55 kV and current of 0.145 mA (µCT 35; Scanco). A three-dimensional Gaussian filter (s = 0.8) with a limited, finite filter support of one was used to suppress noise. A threshold of 342–1000 was used to segment mineralized bone from air and soft tissues. Scanco Medical software was used to determine bone volume.

Mouse tumor histology

Grossly trimmed tibia samples and their encapsulating musculature from each condition were formalin-fixed, decalcified 14% ethylenediaminetetraacetic acid disodium salt dihydrate in paraffin-embedded, and sectioned at 4 µm thickness. Serial sections were used for Hematoxylin and Eosin staining (H&E), immunohistochemistry (IHC), immunofluorescence (IF), and TUNEL assay. All histology samples were evaluated by an expert pathologist.

Confirmation of proliferating cells and cell death were assessed by IF of Ki-67 (Leica, Cat# KI67-MM1-L-CE, 1:300) and DeadEnd Fluorometric TUNEL assay (Promega; Cat #: G3250), respectively, and counterstained with propidium iodide. IHC of CD99 staining was done with rabbit monoclonal CD99 antibody (Abcam EPR3096 1:50), using the SignalStain Boost IHC detection reagent (Cell Signaling Cat #8114), as directed.

All slides were digitally scanned on a Nanozoomer S60 (Hamamatsu) or Axioscan 7 (Zeiss) systems. Measurements of area were made through manual annotations of ROIs on images using NDP.view2 (Hamamatsu).

Electron Microscopy

Duplicate cell monolayers, of each treatment, were grown on MatTek dishes. After an initial wash with PBS, the monolayers were washed with 0.1 M sodium cacodylate and then with 2.5% (v/v) glutaraldehyde in 0.1M sodium cacodylate buffer. After fixation, the monolayers were rinses five times in 0.1 M sodium cacodylate buffer, then were post-fixed in 1% osmium tetroxide and 0.8 % K3[Fe(CN)6] in 0.1 M sodium cacodylate buffer for 1 hour at 4 degrees C. Cells were rinsed with water and en bloc stained with 2% aqueous uranyl acetate overnight at 4 degrees C. After five rinses with water, specimens were dehydrated with increasing

concentration of ethanol at 4 degrees C, infiltrated with Embed-812 resin and polymerized in a 60oC oven overnight. Embed-812 disc were removed from MatTek plastic housing by submerging the dish in liquid nitrogen. Two disc were sandwiched together cell side to cell side by putting a drop of Embed-812 and polymerized in a 60 degree C oven overnight. Sandwiched disc were sectioned perpendicular with a diamond knife (Diatome) on a Leica Ultracut UCT (7) ultramicrotome (Leica Microsystems) and collected onto copper grids, post stained with 2% Uranyl acetate in water and lead citrate. TEM images were acquired on a JEOL-1400 Plus transmission electron microscope equipped with a LaB6 source operated at 120 kV using an AMT-BioSprint 16M CCD camera.

Cells Embedded in 3D Collagen

Collagen gels were created by mixing bovine collagen I (Advanced Biomatrix 5005 and 5026) with concentrated phosphate buffered saline (PBS) and water for a final concentration of 2 mg/mL collagen. This collagen solution was then brought to pH 7 with 1N NaOH and mixed with cells just prior to incubation at 37oC to induce collagen polymerization. Cells were suspended using trypsin/EDTA (Gibco), centrifuged to remove media, and then mixed with collagen just prior to incubation at 37oC to initiate collagen polymerization. Collagen mixed with cells was allowed to polymerize in custom 3D printed mounts for imaging in lightsheet microscopes.

Imaging

Light-sheet fluorescence microscopes were used to image the zebrafish larvae or TC71-AktPH-GFP cells embedded in 3D soft collagen within a custom-made mount. Fixed zebrafish larvae were embedded in 1% low-melting agarose into sonicated, ethanol-washed fluorinated ethylene propylene tubes (Zeus, HS 029EXP/ .018 REC). In this case, the tube is held by a custom-made mount, which allows 3D translation and rotation in our light-sheet microscopes. A conventional mSPIM[62] was used as previously described[39]. Briefly, a 40× NA 0.8 water-dipping objective (CFI Apo NIR 40XW; Nikon Instruments) was used for detection, at room temperature in PBS. A 200-mm focal length tube lens (58-520; Edmund Optics) that formed the image on an sCMOS camera (ORCA-Flash4.0; Hamamatsu Photonics). These conditions provide a resolution of 380 nm laterally and about 1.4 µm axially. A 10× NA 0.28 objective (M Plan Apo 10×, 378-803-3; Mitutoyo) was used for light-sheet illumination. The thickness and the length of the light-sheet were controlled by a variable slit (VA100C; Thorlabs) placed at the conjugate plane of the back focal plane of the illumination objective.

For live imaging on glass, TC71 Cav1-mClover and F-Tractin-GFP cells were mounted on a glass-bottom 35 mm cover dish (MatTek). For GMM staining, TC71 Cav1-mClover cells were incubated with fluorescently tagged Cholera Toxin-B (CT-B) using the Vybrant lipid raft labeling kit, following the manufacturer's protocol (Invitrogen; V34404). Mounted cells were subsequently imaged using a custom-built Oblique Plane Microscope (OPM), as previously described[63]. Briefly, a tilted light sheet was launched after a primary objective (25x NA 1.1, Nikon MRD77220) to illuminate the cells in a glass-bottom dish; the fluorescence was collected by the same objective and formed the image on the camera after passing through the optical train with the magnification of around 43.3. By scanning the light sheet using Galvo mirrors in the optical train, we can rapidly acquire the 3D image of the cells without any mechanical movement of either sample or objective. Also, using a single objective for both illumination and fluorescence collection frees the whole sample space above the objective and makes the system compatible with the standard sample mounting methods. The resolution of the system across the extended FOV was around 0.39, 0.43, and 1.22 μm in the x, y, and z directions, respectively.

Image Analysis

For 3D morphology classifications in zebrafish, images were segmented using the previously established 3D morphology pipeline[64] to segment cell volumes and calculate local membrane curvature from single cell images. For the segmentation process, we smoothed the deconvoluted images with a 3D Gaussian kernel ($\sigma = 3$ pixels) and applied a gamma correction ($\Upsilon = 0.7$), then employed an Otsu threshold, followed by a 3D grayscale flood-fill operation to fill possible holes. The binary images of all cells were visually inspected for segmentation artifacts. Miss-segmented cells were excluded from the data set. Aspect Ratio was calculated on segmented volumes using "regionprops3" in MATLAB. 3D rendering were generated using ChimeraX[65].

To quantify differences in tissue morphology between *CD99 High* and *CD99 Low* cells xenografted in mice, we compared various aspects of nuclear morphology in Hematoxylin and Eosin stained histological slides. First, tumor regions to be analyzed were manually annotated using QuPath[66] on tissue images from 3 slides in each experimental group, scanned at 40X magnification (~0.25 microns/pixel). Second, nuclei in these regions were segmented using the PanNuke version of the HoverNet model as implemented in the TIAToolbox[67]. Third, these images were downsampled to 20X magnification and their color intensities we normalized using the Macenko algorithm[68] against a single (randomly selected) reference slide. Finally, we extracted 37 morphological features relating to size, shape, color, and texture of each individual

nuclei, as previously previously described[69]. All features were then z-score normalized, pooled across slides and a random subset was visualized using T-distributed Stochastic Neighbor Embedding (t-SNE).

For analysis of active PI3K organization on the cell surface, we applied Cellular Harmonics framework[47]. For processing, 3D images underwent Richardson-Lucy deconvolution, with apodization (height parameter -.06) to reduce deconvolution artifacts, smoothing (3D Gaussian kernel, σ=1.5 pixels), and gamma correction (0.7). Segmentation and generation of a triangle mesh to visualize cell surface, and validation was generated using the μshape3D analytical framework[64]. For intensity measurement, we measured the fluorescence intensity local to each mesh vertex from the raw image. The background noise was first removed by subtracting the median pixel intensity outside the cell. Then, at each vertex, the average pixel intensity was computed within a sampling radius of 1 μm over the pixels inside the cell. Finally, we normalized each cell's surface intensity to a mean of one. The calculated values were projected onto the triangular mesh to visualize normalized intensity on the cell surface and rendered using ChimeraX[65]. To calculate spectral decomposition values for each cell, we applied the Laplace-Beltrami operator to the extracted cell surface, as previously described[47], creating a curve of Eigenvalues ordered by increasing frequency. Since the overall intensity of the fluorescence signal often varies between cells due to the concentration of the probes, we first normalized the fluorescence intensity and further calculated an energy density across levels. The energy density reveals that the signal is more uniform when organized across a range of spatial frequencies, and more polarized or patchy when only low-level frequency peaks are detected. Heatmaps in Figure 5C were generated using MATLAB to visualize and compare the energy density curves of individual cells between experimental groups. Statistical differences were calculated using a permutation test comparing the Mean Absolute Deviation between rows in the heatmaps.

For GM1 image analysis, segmented image pseudo-colored by timepoint were generated using the "Analyze Particles" tool followed by the Temporal-Color Code plug-in in ImageJ. Quantification of dynamics of GM1 puncta over time was measured by sum of absolute differences in segmented area between time frames.

Plots and statistical tests were visualized and preformed using GraphPad Prism.

ACKNOWLEDGMENTS

We would like to thank UT Southwestern Whole Brain Microscopy Facility (grant award number 1S10OD032267-01 to Denise Ramirez), Histo Pathology Core Facility, and Quantitative Light Microscopy Core Facility, for their contributions to this work.

Funding for this work in the Danuser lab has been provided through R35 GM136428 (National Institute of General Medical Sciences) and microscope development in the Fiolka lab has been supported by R33 CA235254 (National Cancer Institute). D. Segal acknowledges funding from European Molecular Biology Organization Long-term Research Fellowship (ALTF 626-2018). X. Wang and N.S. Williams acknowledge funding from the NCI (1U54CA231649) and institutional support from UTSW for the Preclinical Pharmacology Core.

The authors declare no competing financial interests.

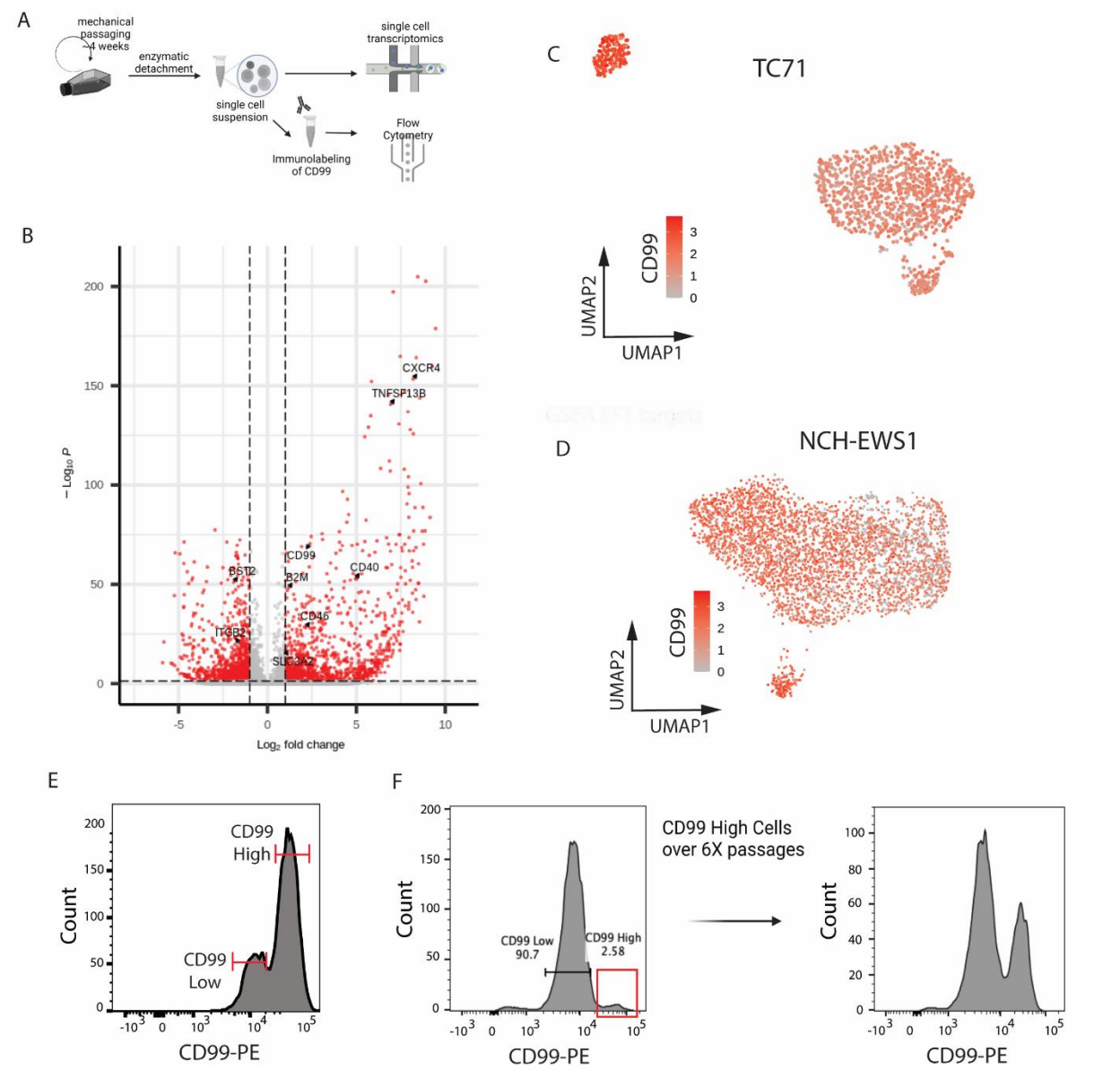

Figure 1: High CD99 marks a distinct Ewing Sarcoma cell state. (A) Schematic illustrating the experimental workflow. After approximately four weeks of mechanical passaging to preserve surface receptors, cells are enzymatically detached from dish and prepared in a single cell suspension for single cell RNA seq (scRNA-seq) to profile receptor expression, or immunolabeling of target receptor for flow cytometry. **(B)** Volcano plot depicting differential expression of distinct cluster (cluster 2 in Figure S1A) compared to all other cells, as measured by scRNA-seq. Differentially expressed receptors are highlighted. **(C-D)** UMAP visualization with log normalized expression of CD99 of TC71 cells. **(c)**, or in NCH-EWS1 patient-derived xenograft (PDX) cells **(d)**, analyzed by scRNA-seq. **(E)** Flow cytometry histogram depicting relative intensity of CD99-PE conjugated antibody, displaying a bimodal distribution of *CD99 High* and *CD99 Low* cell populations. Red bars indicate populations isolated by flow cytometry for further characterization. **(F)** *CD99 High* cells, detected by flow cytometry (left histogram, subpopulation outlined in red), and subsequently isolated and passaged six times, then reevaluated by the same assay (right histogram). The recurrent bimodal distribution of CD99

expression suggests that *CD99 High* cells can shift between *CD99 High* and *CD99 Low* cell states. Bars and numbers indicate the cell population in *CD99 High* or *CD99 Low* state.

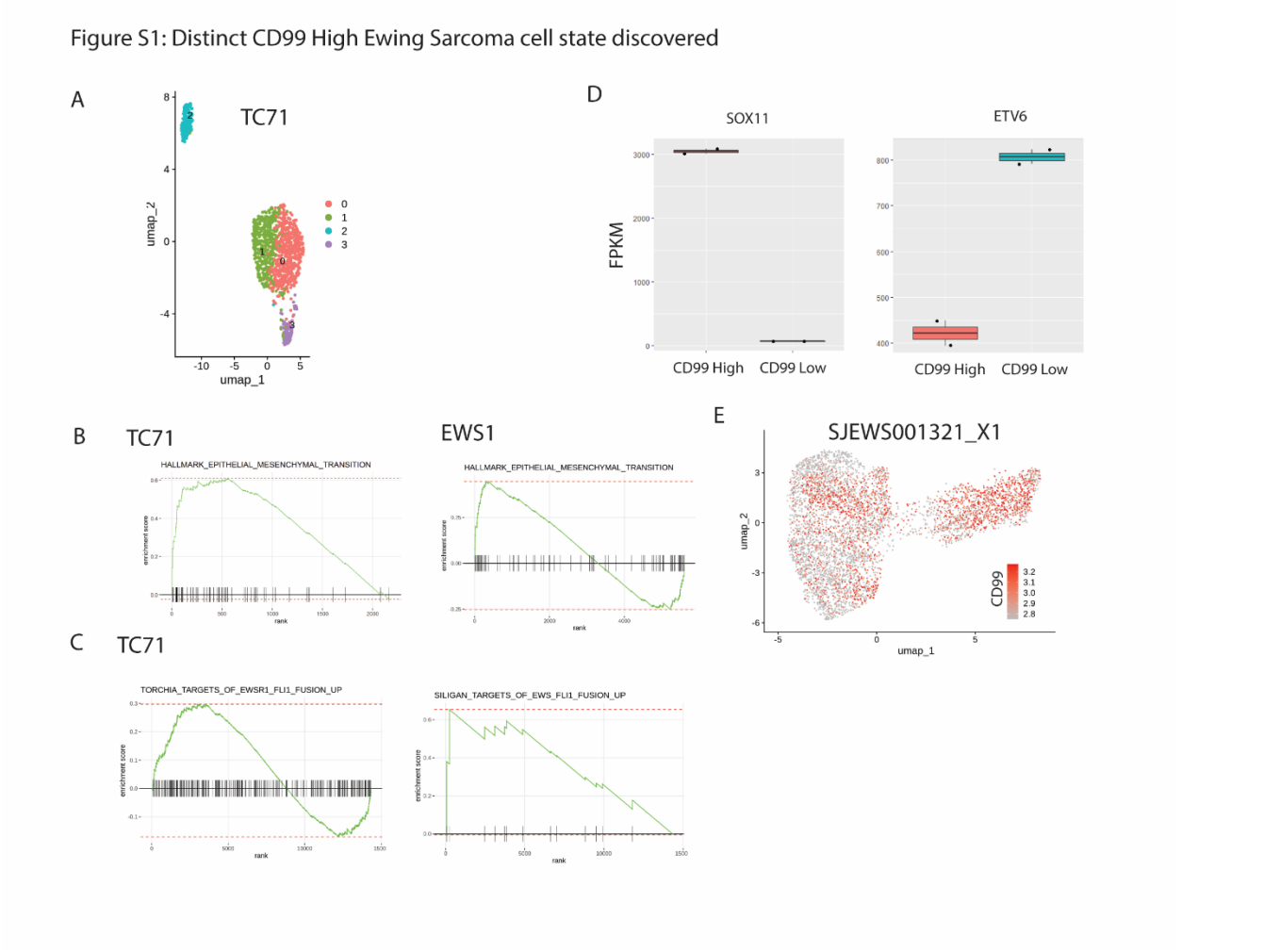

Figure S1 (related to Figure 1): High CD99 marks a distinct Ewing Sarcoma cell state. (A) UMAP visualization of TC71 cells analyzed by scRNA-seq, with cluster numbers annotated. We identified a cluser (cluster 2) with a distinct transcriptional profile (see figure 1C). **(B)** Gene Set Enrichment Analysis (GSEA) plot of Cluster 2 vs. all other cluster shows enrichment in *CD99 High* cluster for an Epithelial-to-Mesenchymal-Transition (EMT) gene signature in TC71 (NES = 2.1, p-value<.001) and NCH-EWS1 (NES = 1.5, p-value = 0.01) cells. **(C)** GSEA plots showing no clear enrichment in TC71 cells of *CD99 High* cluster vs. other cells in expression of known EWSR2::FLI1 gene signatures (Torchia NES = 1.04, p-value>.1, Siligan NES = 1.48, p-value =0.05) **(D)** Boxplots depicting bulk RNA expression differences of ETV6 and SOX11 between *CD99 High* and *CD99 Low* cells. **(E)** UMAP visualization with log normalized expression of CD99 of SJEWS001321_X1 PDX cells, analyzed by scRNA-seq.

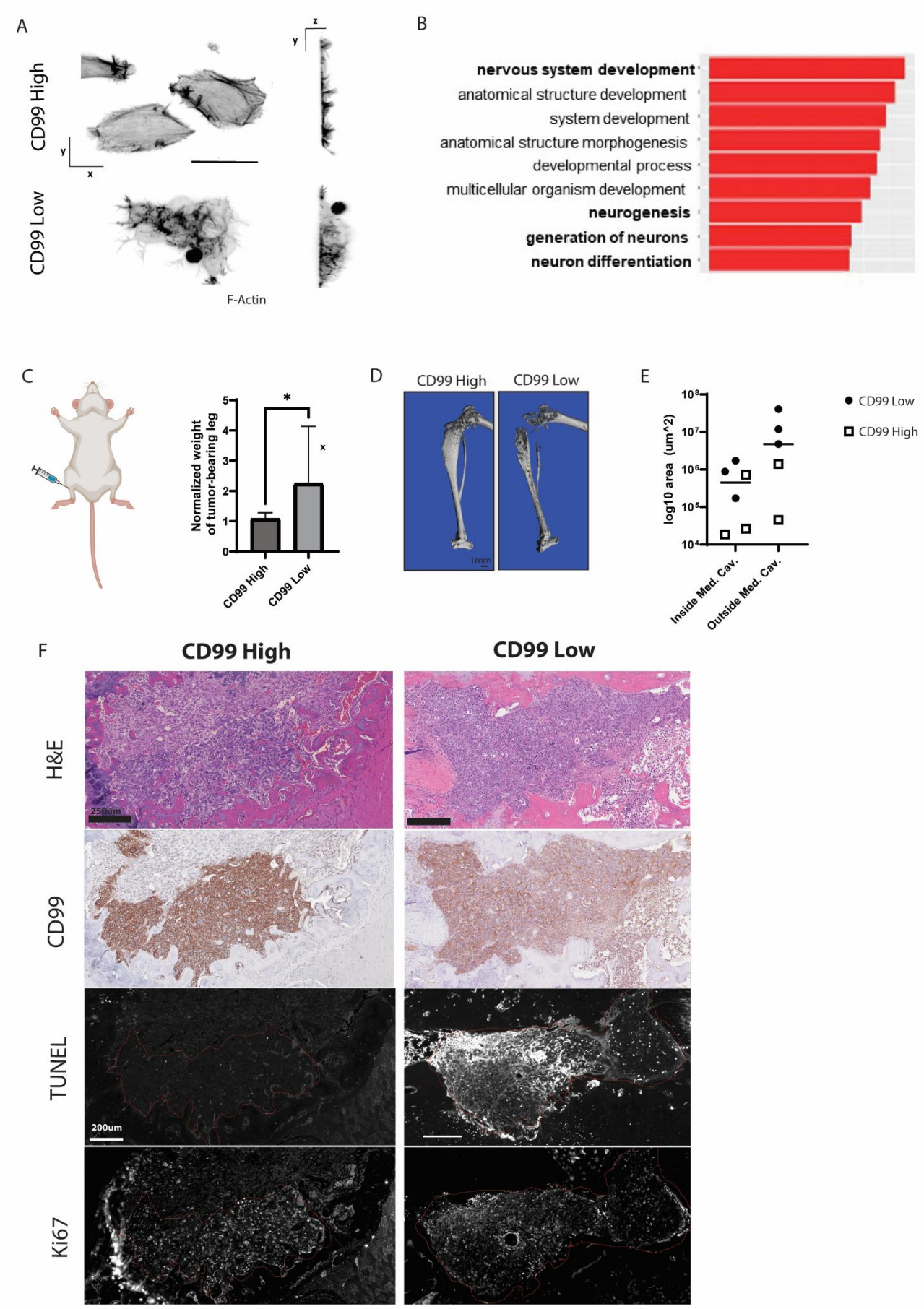
A
CD99 High
CD99 Low
F-Actin
B
nervous system development
anatomical structure development
system development
anatomical structure morphogenesis
developmental process
multicellular organism development
neurogenesis
generation of neurons
neuron differentiation
C
Normalized weight of tumor-bearing leg
CD99 High
CD99 Low
D
CD99 High
CD99 Low
1mm
E
log10 area (um^2)
Inside Med. Cav.
Outside Med. Cav.
CD99 Low
CD99 High
F
CD99 High
CD99 Low
H&E
CD99
TUNEL
Ki67
250um
200um

Figure 2 (above): *CD99 High and Low* cells display differences in morphology, gene expression, and survival. (A) Maximum Intensity Projections in XY view (left) or YZ view (right) of *CD99 Low* and *CD99 High* TC71 cells expressing F-Actin marker F-Tractin-GFP and imaged using oblique plane microscopy in adherent culture display distinct cell morphologies (scale bar = 50um). **(B)** Gene Ontology terms enriched in *CD99 High* cells show enrichment of neurally differentiated gene signatures. **(C)** (left) Schematic depicting intratibial xenografts of *CD99 High* or *CD99 Low* TC71 cells into immunocompromised mice. (right) Graph depicting weight of tumor-bearing leg normalized to the weight of non-tumor bearing leg of same mouse in *CD99 High* (n=6) or *CD99 Low* (n=6) xenografts(asterisk depicts $p>0.05$, t-test). **(D)** Representative computer tomography scan of tumor bearing legs depicting differences in presence of bony destruction caused by tumor cells. **(E)** Manual analysis of the area observed by histological sections inside the medullary cavity (Med. Cav.) of the bone, or outside of the Med. Cav., such as within the surrounding muscle. Note that while *CD99 Low* cells have larger clusters outside the Med. Cav., *CD99 High* cells have comparably smaller clusters in both areas (n = 3 mice). **(F)** Histological sections of intratibial xenografts in immunocompromised mice, showing tumor-bearing areas within the med. Cav. of either *CD99 High* or *CD99 Low* cells, labeled with H&E, chemically immunostained for CD99, and fluorescently stained for the apoptotic marker TUNEL or the proliferative marker Ki67 in serial sections. Note the decreased TUNEL staining observed in the *CD99 High* tumor compared to *CD99 Low* tumor.

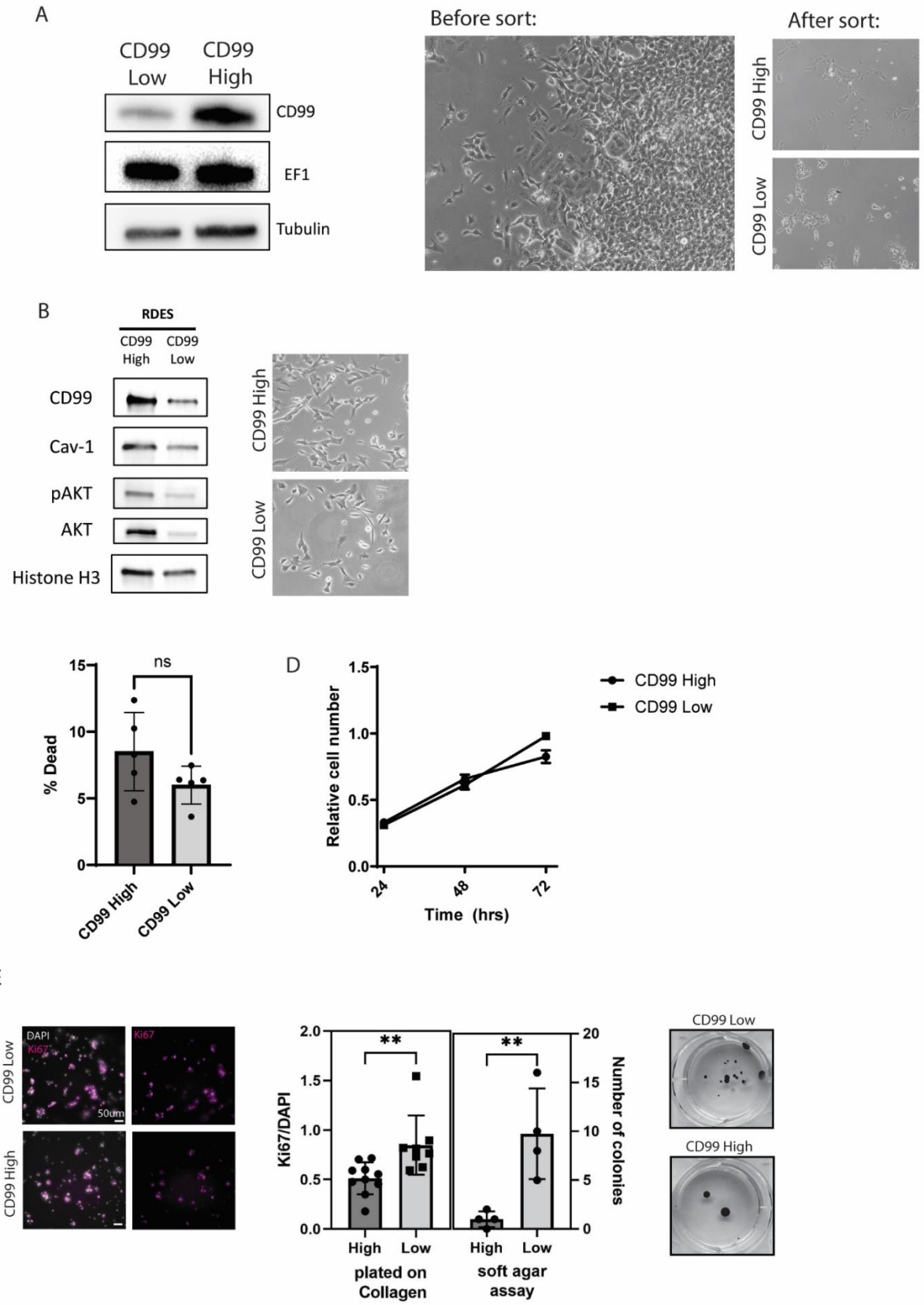
A
CD99 Low
CD99 High
CD99
EF1
Tubulin
Before sort:
After sort:
CD99 High
CD99 Low
B
RDES
CD99 High
CD99 Low
CD99
Cav-1
pAKT
AKT
Histone H3
CD99 High
CD99 Low
C
ns
% Dead
15
10
5
0
CD99 High
CD99 Low
D
Relative cell number
1.5
1.0
0.5
0.0
24
48
72
Time (hrs)
CD99 High
CD99 Low
E
CD99 Low
CD99 High
DAPI
Ki67
Ki67
50um
Ki67/DAPI
2.0
1.5
1.0
0.5
0.0
**
**
Number of colonies
20
15
10
5
0
High
Low
High
Low
plated on Collagen
soft agar assay
CD99 Low
CD99 High

Figure S2 (related to Figure 2): *CD99 High* and *Low* cells display differences in morphology, gene expression, and survival. (A) (left) Western blot depicting differences in CD99 expression but not EWS:FLI1 (EF1) expression between *CD99 High* and *CD99 Low* TC71 cells. (right) Brightfield images showing mixed TC71 cell morphologies observed before flow cytometric sorting, and distinct cell morphologies observed after sorting by flow cytometry. **(B)** Western blot (left) and brightfield images (right) depicting differences in protein expression and morphology, respectively, between *CD99 High* and *CD99 Low* RDES cells. **(C-D)** No differences are observed in cell survival, measured by integration of Ethidium Homodimer (C) or proliferation, measured by a cell viability assay (D) in TC71 cells grown in adherent culture conditions. **(E)** Cells plated on Collagen and stained for proliferation marker Ki67 (left) or soft agar assays (right) show significantly slower growth of *CD99 High* cells in soft environments (**, $p>0.005$, t-test).

Figure S3: Phenotypes of different states

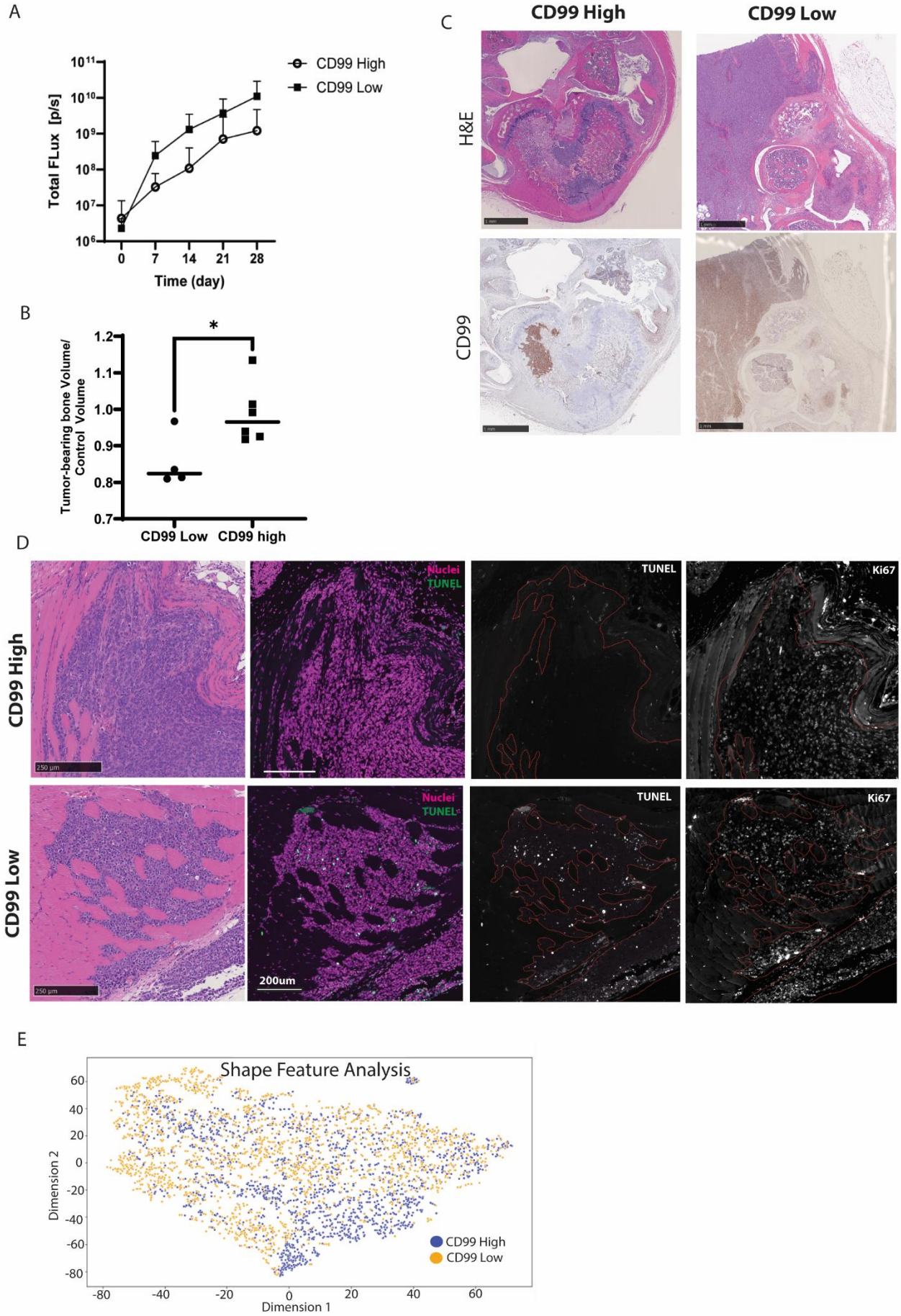

Figure S3 (related to Figure 2): *CD99 High* cells display differences in morphology, gene expression, and survival. (A) Total bioluminescent flux of TC71 *CD99 High* (n=6) or *CD99 Low* (n=6) luciferase-expressing cells, in intratibial xenografts of immunocompromised mice, measured over time. Difference between curves is statistically significant ($p<0.05$, mixed-effect analysis). **(B)** Volume measurements from computed tomography bone scan of tumor-bearing leg normalized by volume of non-tumor-bearing leg, in intratibial xenografts. Note that legs xenografted with *CD99 High* (n = 6) cells display higher normalized volume compared to *CD99 Low* (n=4) cells, suggesting reduced bony destruction ($p<0.05$, t-test). **(C)** Representative histological sections of intratibial xenografts, showing tumor-bearing areas of either *CD99 High* or *CD99 Low* cells, labeled with H&E (top), or chemically immunostained for CD99 (bottom). Note the relatively large tumor outside of the medullary cavity (med. cav.) and in the surrounding skeletal muscle in the *CD99 Low* tumor, with smaller tumor masses within the med. cav. In contrast, the *CD99 High* tumor is present only in a relatively small area within the med. cav. **(D)** Histological sections of intratibial xenografts in immunocompromised mice, showing tumor-bearing areas outside the med. Cav. of either *CD99 High* or *CD99 Low* cells, labeled with H&E, and fluorescently stained for the apoptotic marker TUNEL or the proliferative marker Ki67, and with a propidium iodide nuclear counter stain, in serial sections. Note the decreased TUNEL staining observed in the *CD99 High* tumor compared to *CD99 Low* tumor. **(E)** tSNE visualization of shape feature analysis on histological H&E-stained sections of intratibial xenografts of *CD99 High* or *CD99 Low* cells uncovers differences in cell morphology between the two experimental groups.

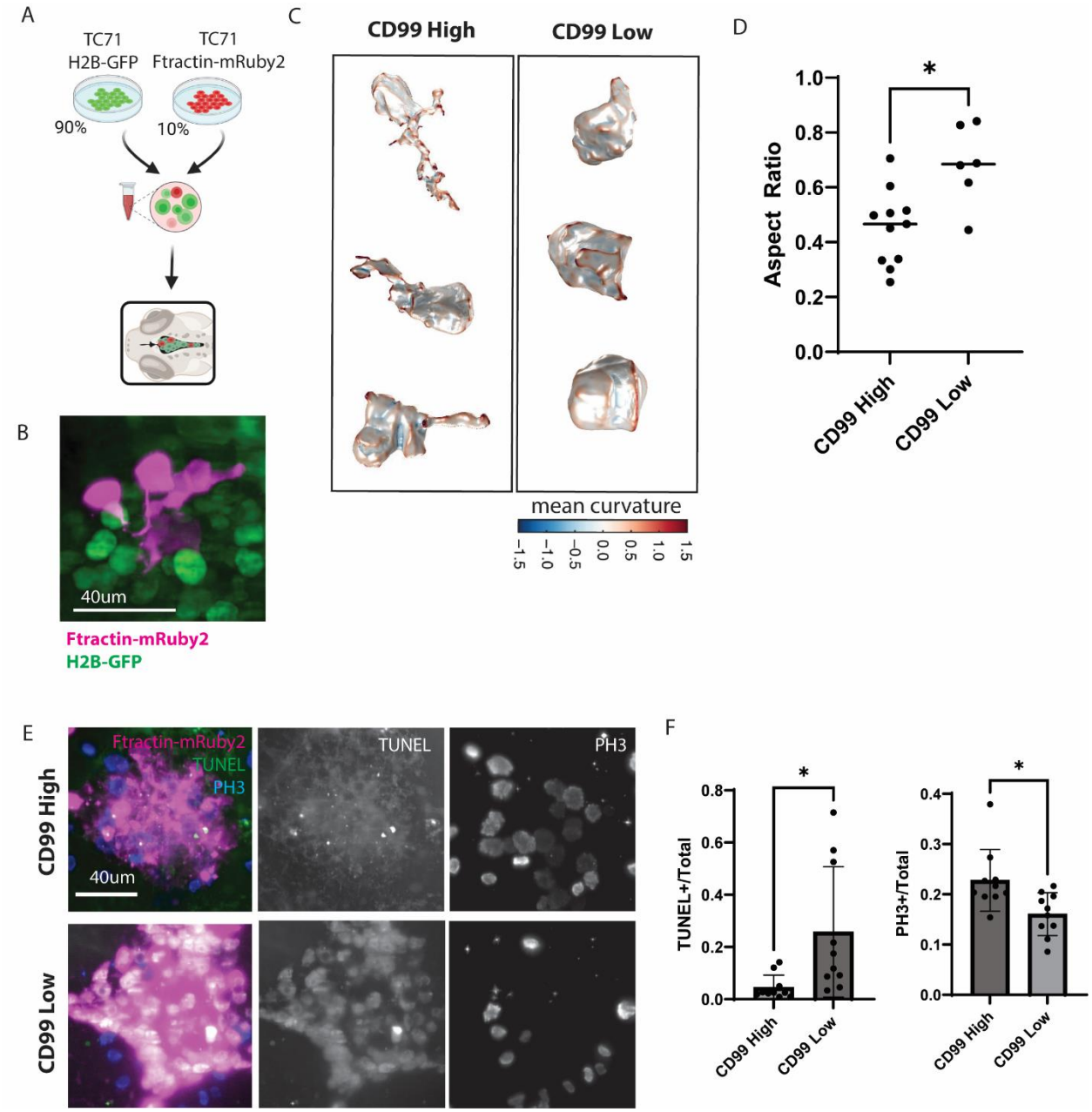

Figure 3: *CD99 High* and *Low* cells display differences in morphology and survival in zebrafish xenografts. (A) Schematic of experimental set-up to identify single-cell morphologies in xenografted cells within the hindbrain ventricle (HBV) of zebrafish larvae. In order to distinguish single-cell morphologies of individual cells, we prepared a mosaic cell mixture consisting of 90% of TC71 unsorted cells expressing the fluorescently-tagged nuclear marker H2B-GFP, and 10% of TC71 *CD99 High* or *CD99 Low* cells expressing the F-actin marker Ftractin-mRuby2. **(B)** Maximum Intensity Projection of TC71 cells within the HBV expressing F-Tractin-mRuby2 (magenta) or H2B-GFP (green). **(C)** Representative 3D volume renderings of single cells, pseudocolored by local membrane curvature (1 um^{-1}). Note the highly elongated and protrusive shapes observed in *CD99 High* cells. **(D)** Plot depicting differences in aspect ratio of individual cells, as a metric of differences in cell shape in *CD99 High* (n = 11 cells) and

CD99 Low (n=6 cells) (p-value<0.5, t-test). **(E)** TC71 *CD99 High* or *CD99* Low cells expressing F-tractin-mRuby2 (magenta) were injected into the HBV of zebrafish larvae, and stained for apoptotic marker TUNEL (green (left), grey (middle)) and proliferative marker Phospho-histone H3 (PH3, blue (left), grey (right)) 48hrs post-injection. Maximum Intensity Projections show increased TUNEL staining in *CD99 Low* cells. **(F)** Proportion of measured area of TUNEL-positive (left) or PH3-positive (right) signal overlapping with F-Tractin-mRub2 expressing cells. Note decreased cell death and higher proliferation in *CD99 High* cells.

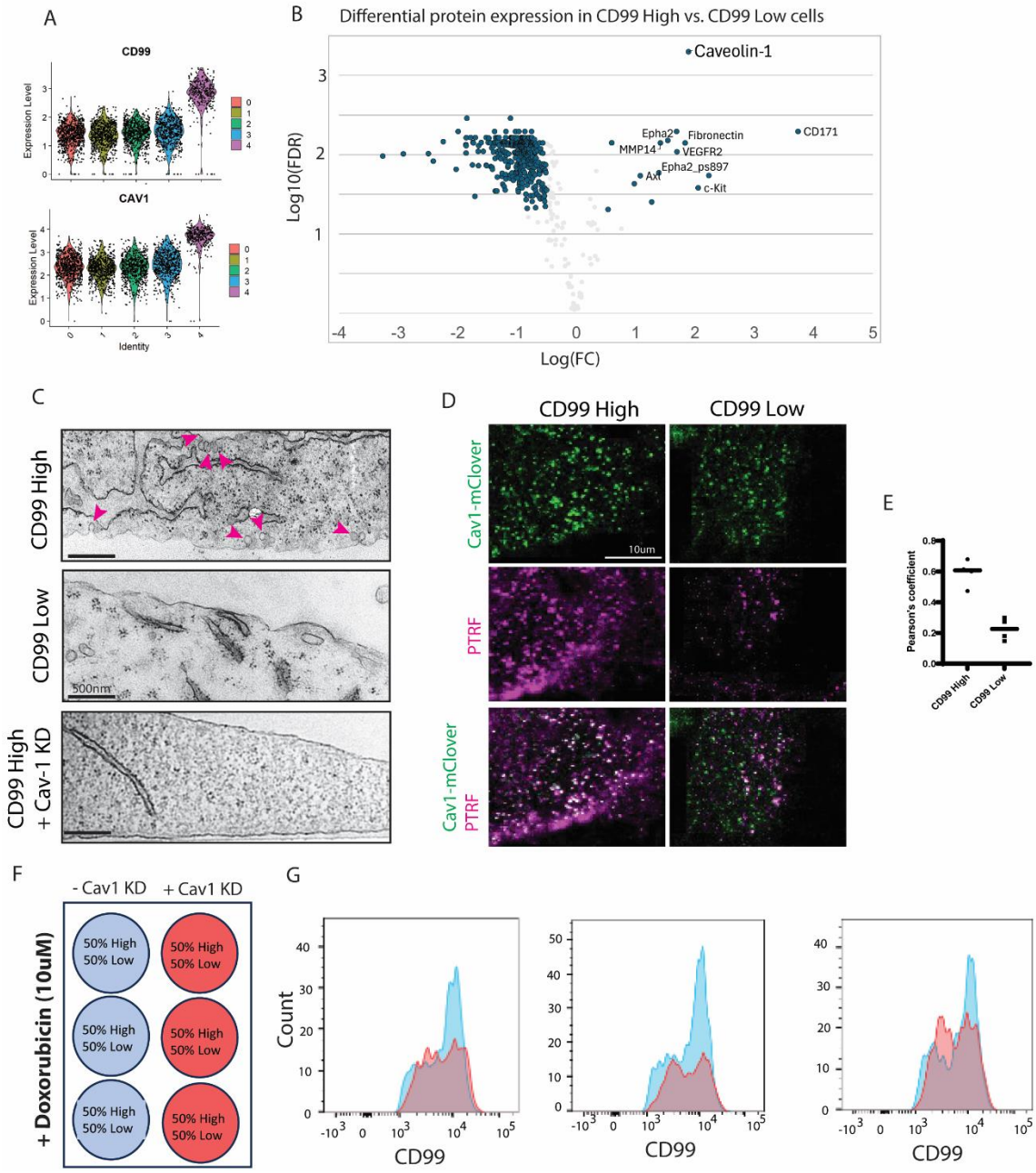

Figure 4: Caveolin-1 emerges as a potential driver of functions associated with the *CD99 High* State. (A) RNA expression differences of CD99 and Cav1 between different clusters, analyzed from scRNA-seq data (see Fig S1). **(B)** Volcano plot of differential protein expression

between *CD99 Low* vs. *CD99 High* cells, analyzed by Reverse Phase Protein Array. **(C)** Representative scanning electron microscope images of *CD99 High*, *CD99 Low*, and *CD99 High* cells expressing inducible Cav-1 shRNA (Cav1 KD). Magenta arrowheads highlight observed caveolae in *CD99 High* cells. **(D)** Representative images of TC71 *CD99 High* or *CD99 Low* cells with endogenous expression for Cav1-mClover, and immunostained for PTRF show colocalization of Cav1 and PTRF in *CD99 High* but not *CD99 Low* cells. **(E)** Quantification of colocalization of PTRF and Cav-1 in *CD99 High* and *CD99 Low* cells, calculated by Pearson's coefficient. **(F)** Experimental setup for a flow cytometry assay of a mixture of *CD99 High* and *CD99 Low* cells, with or without knockdown of Cav-1, grown with Doxorubicin (10uM). **(G)** Histogram depicting relative intensity as measured by flow cytometry of TC71 *CD99 High/Low* cell mixture treated with Doxorubicin and fluorescently stained for CD99 on cell surface, with (red) or without (blue) Cav1 knockdown (Cav1 KD). The *CD99 High* peak is lost upon Cav1 KD.

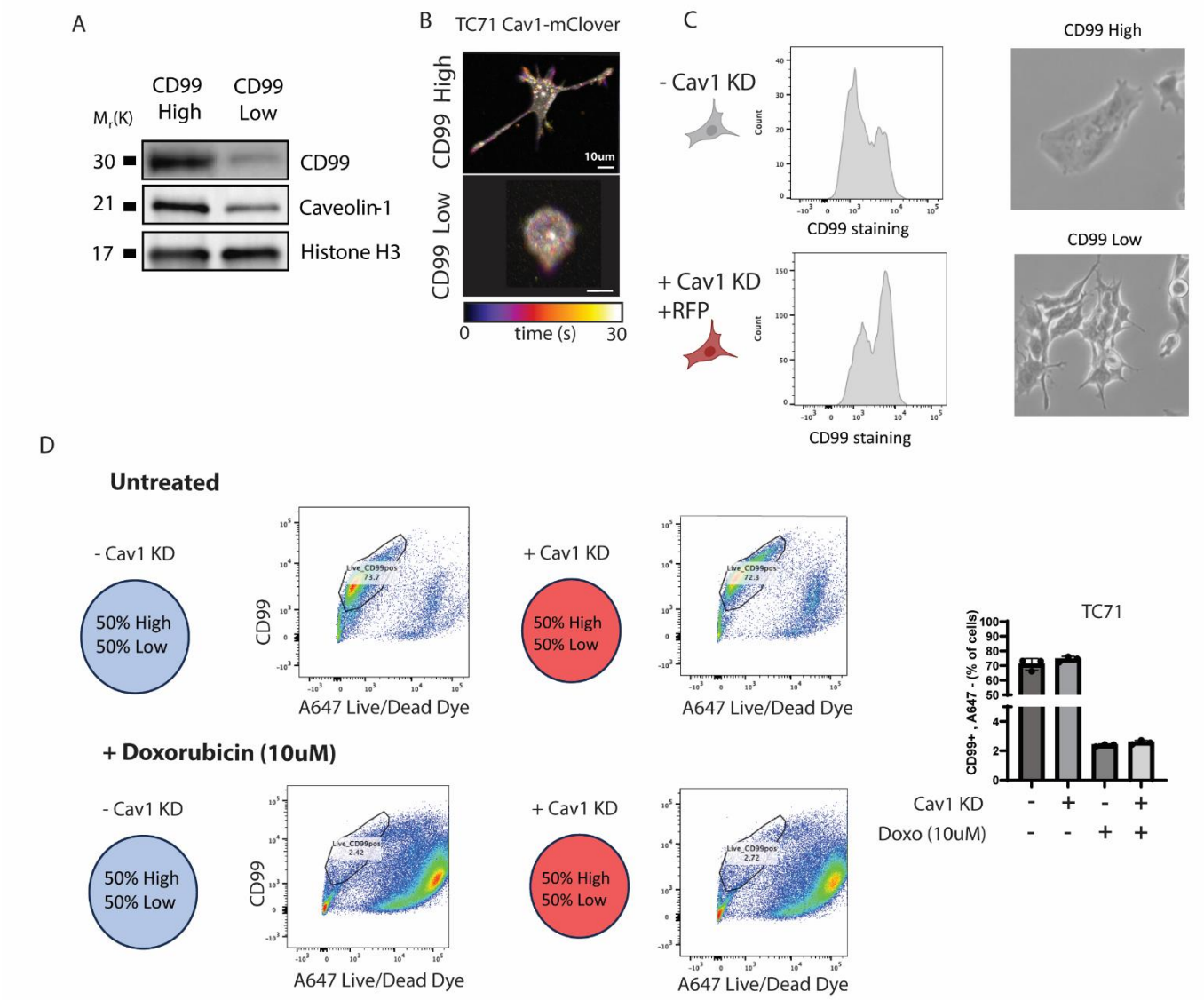

Figure S4 (related to Figure 4): Caveolin-1 emerges as a potential driver of *CD99 High* State. (A) Western blot showing higher Cav-1 protein levels in *CD99 High* cells. **(B)** Live imaging of TC71 *CD99 High* and *CD99 Low* cells, expressing endogenously tagged Cav1-mClover. Sequences were acquired over 30 seconds with 2 second time intervals. Representative XY maximum intensity projections of raw image pseudo-colored by timepoint demonstrates dynamics of Cav1 puncta over time. **(C)** (Left) Flow cytometry intensity plot measuring CD99 in mixture of TC71 cells with (red) or without (grey) inducible Cav-1 shRNA (Cav-1 KD), combined with an RFP reporter. Note the increase in measured *CD99 High* cells upon Cav-1 KD. (Right) Brightfield images showing unchanged differential cell morphology between *CD99 High* and *CD99 Low* cells upon Cav-1 KD. **(D)** (left, middle) Flow cytometry-based viability assay of a mixture of *CD99 High* and *CD99 Low* cells, with (red) or without (blue) Cav-1 KD, untreated (top) or grown with Doxorubicin (10uM, bottom). The x-axis shows measurement of the A647-Live/Dead viability dye, while the y-axis shows measured intensity of CD99. The CD99+, A647 negative population is outlined. (right) Overall survival of cells, as detected by CD99+, A647- population. with or without drug treatment and with or without Cav-1 KD.

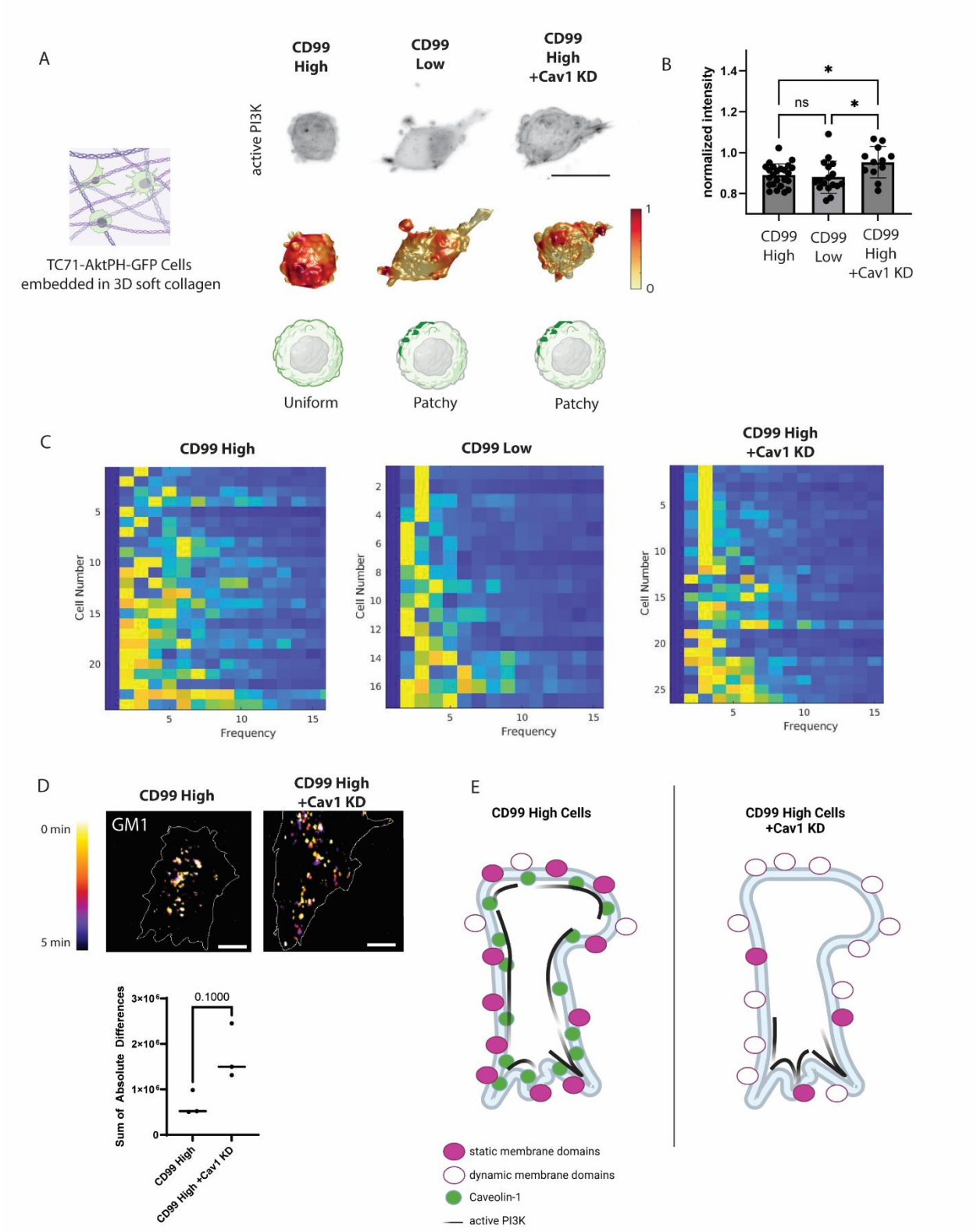
A
TC71-AktPH-GFP Cells
embedded in 3D soft collagen
CD99 High
CD99 Low
CD99 High +Cav1 KD
active PI3K
1
0
Uniform
Patchy
Patchy
B
normalized intensity
1.4
1.2
1.0
0.8
ns
*
*
CD99 High
CD99 Low
CD99 High +Cav1 KD
C
CD99 High
CD99 Low
CD99 High +Cav1 KD
Cell Number
Frequency
D
CD99 High
CD99 High +Cav1 KD
0 min
5 min
GM1
Sum of Absolute Differences
3×10⁶
2×10⁶
1×10⁶
0
0.1000
CD99 High
CD99 High +Cav1 KD
E
CD99 High Cells
CD99 High Cells +Cav1 KD
static membrane domains
dynamic membrane domains
Caveolin-1
active PI3K

Figure 5: Caveolin-1 regulates PI3K/AKT signaling in *CD99 High* Cells. (A) TC71 *CD99 High* and *CD99 Low* cells*, and CD99 High* cells +Cav1 KD, expressing PI3K activation sensor AktPH-GFP. For imaging cells were embedded in soft collagen. (Top) Maximum Intensity Projection of raw data (scale bar 20um). (Middle) surface rendering of the same cell, with localization of PI3K activity projected onto the 3D cell surface. Red surface regions indicate high local PI3K activity. (Bottom) Schematics showing uniform or patchy PI3K activity distribution observed in each experimental group. **(B)** PI3K activity measured as total sum intensity on the cell surface normalized to mean intensity of cell volume. Note the slight increase of total PI3K activity in *CD99 High* + Cav1 KD (n = 24, 17, and 12 cells, for CD99 High, CD99 Low, and CD99 High +Cav1 KD, respectively. * p-value<0.05, Tukey's multiple comparisons test). **(C)** Heatmaps depicting normalized Energy Density of measured cells across increasing spatial frequency levels, as a measure of the distribution pattern of active PI3K on the cell surface. Each row is normalized to 1 and represents a single cell. Highly polarized cells display a single high Energy Density (yellow) peak only at lower frequencies, while a cell with more uniform signal distribution display several smaller Energy Density peaks across frequencies. *CD99 High* cells show a more uniform distribution of active PI3K, as measured by Energy Density, compared to *CD99 Low* cells. *CD99 High* cells +Cav1 KD show more polarized signal distributions, similarly to *CD99 Low* cells and significantly different from *CD99 High* cells (permutation p-value =.02, Mean Absolute Deviation). **(D)** (top) Live imaging of TC71 *CD99 High* and *CD99 Low* cells, stained with fluorescently tagged Cholera-Toxin B subunit (CTxB) to label GM1 glycosphingolipid, imaged with oblique plane microscopy. Sequences were acquired over 5min with 30 second time intervals. Representative XY maximum intensity projections of segmented image pseudo-colored by timepoint demonstrates dynamics of GM1 puncta over time. (bottom) Quantification of dynamics of GM1 puncta over time, as measured by sum of absolute differences between frames (N = 3 cells). **(E)** Schematic representing findings. *CD99 High* cells have high expression of Cav-1 and many caveolae to organize the membrane through stabilization of lipid nanodomains such as GM1 and others. These make docking sites promiscuously available to PI3K localization, enhancing opportunities for stable signaling across the entire cell surface. *CD99 Low* cells, or *CD99 High* cells with reduced Cav-1 expression, have dynamic, less stable nanodomains which do not serve as stable signaling hubs, and instead PI3K localization is concentrated to areas of high local curvature such as protrusions, as described in other works.

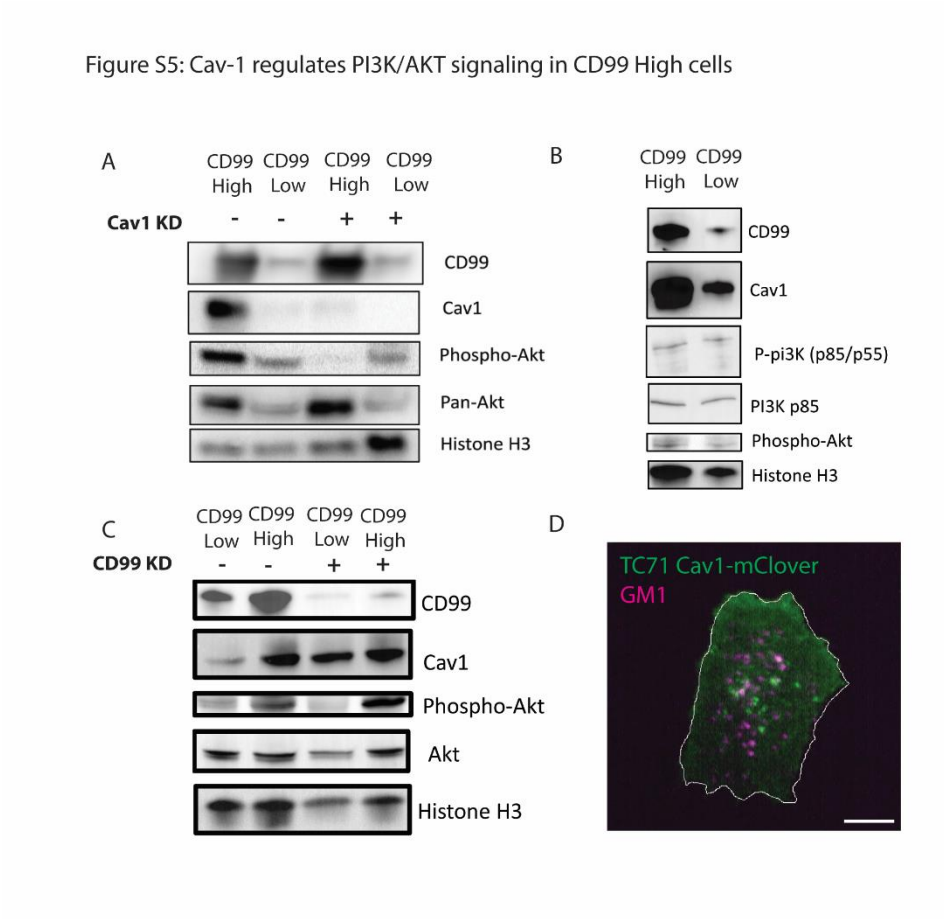

Figure S5 (related to Figure 5): Cav-1 regulates PI3K/AKT signaling in *CD99 High* cells. **(A)** Western blot depicting high Cav1 expression and increased active AKT signaling in *CD99 High* cells, which is lost upon Cav-1 KD. **(B)** Western blot depicting no change in detected levels of active PI3K between experimental groups. **(C)** Western blot showing inducible expression of CD99 shRNA (CD99 KD) does not reduce Cav1 expression or inhibit active AKT, suggesting that CD99 is not involved in regulating this pathway. **(D)** Maximum Intensity Projection of TC71 cells expressing Cav1-mClover (green) and stained with fluorescently tagged Cholera-Toxin B subunit (CTxB) to label GM1 glycosphingolipid (magenta). Note little to no observed colocalization between the puncta of the two labeled elements.

1. Hanahan, D. & Weinberg, R.A. Hallmarks of cancer: the next generation. *Cell* **144**, 646-674 (2011).
2. Quintanal-Villalonga, A. *et al.* Lineage plasticity in cancer: a shared pathway of therapeutic resistance. *Nat Rev Clin Oncol* **17**, 360-371 (2020).
3. Grobner, S.N. *et al.* The landscape of genomic alterations across childhood cancers. *Nature* **555**, 321-327 (2018).
4. Crompton, B.D. *et al.* The genomic landscape of pediatric Ewing sarcoma. *Cancer Discov* **4**, 1326-1341 (2014).
5. Grunewald, T.G.P. *et al.* Ewing sarcoma. *Nat Rev Dis Primers* **4**, 5 (2018).
6. Delattre, O. *et al.* The Ewing family of tumors--a subgroup of small-round-cell tumors defined by specific chimeric transcripts. *N Engl J Med* **331**, 294-299 (1994).
7. Aynaud, M.M. *et al.* Transcriptional Programs Define Intratumoral Heterogeneity of Ewing Sarcoma at Single-Cell Resolution. *Cell Rep* **30**, 1767-1779 e1766 (2020).
8. Franzetti, G.A. *et al.* Cell-to-cell heterogeneity of EWSR1-FLI1 activity determines proliferation/migration choices in Ewing sarcoma cells. *Oncogene* **36**, 3505-3514 (2017).
9. Wrenn, E.D. *et al.* Cancer-Associated Fibroblast-Like Tumor Cells Remodel the Ewing Sarcoma Tumor Microenvironment. *Clin Cancer Res* **29**, 5140-5154 (2023).
10. Gao, Y. *et al.* ETV6 dependency in Ewing sarcoma by antagonism of EWS-FLI1-mediated enhancer activation. *Nat Cell Biol* **25**, 298-308 (2023).
11. Lu, D.Y. *et al.* The ETS transcription factor ETV6 constrains the transcriptional activity of EWS-FLI to promote Ewing sarcoma. *Nat Cell Biol* **25**, 285-297 (2023).
12. Bankaitis, V.A., Mousley, C.J. & Schaaf, G. The Sec14 superfamily and mechanisms for crosstalk between lipid metabolism and lipid signaling. *Trends Biochem Sci* **35**, 150-160 (2010).
13. Grecco, H.E., Schmick, M. & Bastiaens, P.I. Signaling from the living plasma membrane. *Cell* **144**, 897-909 (2011).
14. Anderson, R.G. The caveolae membrane system. *Annu Rev Biochem* **67**, 199-225 (1998).
15. Couet, J., Sargiacomo, M. & Lisanti, M.P. Interaction of a receptor tyrosine kinase, EGF-R, with caveolins. Caveolin binding negatively regulates tyrosine and serine/threonine kinase activities. *J Biol Chem* **272**, 30429-30438 (1997).
16. Couet, J., Li, S., Okamoto, T., Ikezu, T. & Lisanti, M.P. Identification of peptide and protein ligands for the caveolin-scaffolding domain. Implications for the interaction of caveolin with caveolae-associated proteins. *J Biol Chem* **272**, 6525-6533 (1997).
17. Garcia-Cardena, G. *et al.* Dissecting the interaction between nitric oxide synthase (NOS) and caveolin. Functional significance of the nos caveolin binding domain in vivo. *J Biol Chem* **272**, 25437-25440 (1997).
18. Galbiati, F. *et al.* Caveolin-1 expression inhibits Wnt/beta-catenin/Lef-1 signaling by recruiting beta-catenin to caveolae membrane domains. *J Biol Chem* **275**, 23368-23377 (2000).
19. Labrecque, L. *et al.* Src-mediated tyrosine phosphorylation of caveolin-1 induces its association with membrane type 1 matrix metalloproteinase. *J Biol Chem* **279**, 52132-52140 (2004).
20. Gottlieb-Abraham, E. *et al.* Src-mediated caveolin-1 phosphorylation affects the targeting of active Src to specific membrane sites. *Mol Biol Cell* **24**, 3881-3895 (2013).
21. Campos, A. *et al.* Cell Intrinsic and Extrinsic Mechanisms of Caveolin-1-Enhanced Metastasis. *Biomolecules* **9** (2019).
22. Nunez-Wehinger, S. *et al.* Caveolin-1 in cell migration and metastasis. *Curr Mol Med* **14**, 255-274 (2014).

23. Sainz-Jaspeado, M. *et al.* Caveolin-1 modulates the ability of Ewing's sarcoma to metastasize. *Mol Cancer Res* **8**, 1489-1500 (2010).
24. Lagares-Tena, L. *et al.* Caveolin-1 promotes Ewing sarcoma metastasis regulating MMP-9 expression through MAPK/ERK pathway. *Oncotarget* **7**, 56889-56903 (2016).
25. Yeh, Y.C., Ling, J.Y., Chen, W.C., Lin, H.H. & Tang, M.J. Mechanotransduction of matrix stiffness in regulation of focal adhesion size and number: reciprocal regulation of caveolin-1 and beta1 integrin. *Sci Rep* **7**, 15008 (2017).
26. Goetz, J.G. *et al.* Biomechanical remodeling of the microenvironment by stromal caveolin-1 favors tumor invasion and metastasis. *Cell* **146**, 148-163 (2011).
27. Sinha, B. *et al.* Cells respond to mechanical stress by rapid disassembly of caveolae. *Cell* **144**, 402-413 (2011).
28. Ariotti, N. *et al.* Caveolae regulate the nanoscale organization of the plasma membrane to remotely control Ras signaling. *J Cell Biol* **204**, 777-792 (2014).
29. Zhang, B. *et al.* Caveolin-1 phosphorylation is required for stretch-induced EGFR and Akt activation in mesangial cells. *Cell Signal* **19**, 1690-1700 (2007).
30. Yang, H. *et al.* Mechanosensitive caveolin-1 activation-induced PI3K/Akt/mTOR signaling pathway promotes breast cancer motility, invadopodia formation and metastasis in vivo. *Oncotarget* **7**, 16227-16247 (2016).
31. Zhou, Y. *et al.* Caveolin-1 and cavin1 act synergistically to generate a unique lipid environment in caveolae. *J Cell Biol* **220** (2021).
32. Zipori, D., Friedman, A., Tamir, M., Silverberg, D. & Malik, Z. Cultured mouse marrow cell lines: interactions between fibroblastoid cells and monocytes. *J Cell Physiol* **118**, 143-152 (1984).
33. Zipori, D., Toledo, J. & von der Mark, K. Phenotypic heterogeneity among stromal cell lines from mouse bone marrow disclosed in their extracellular matrix composition and interactions with normal and leukemic cells. *Blood* **66**, 447-455 (1985).
34. Zipori, D. The nature of stem cells: state rather than entity. *Nat Rev Genet* **5**, 873-878 (2004).
35. Hancock, J.D. & Lessnick, S.L. A transcriptional profiling meta-analysis reveals a core EWS-FLI gene expression signature. *Cell Cycle* **7**, 250-256 (2008).
36. Chaturvedi, A., Hoffman, L.M., Welm, A.L., Lessnick, S.L. & Beckerle, M.C. The EWS/FLI Oncogene Drives Changes in Cellular Morphology, Adhesion, and Migration in Ewing Sarcoma. *Genes Cancer* **3**, 102-116 (2012).
37. Riggi, N. *et al.* EWS-FLI-1 expression triggers a Ewing's sarcoma initiation program in primary human mesenchymal stem cells. *Cancer Res* **68**, 2176-2185 (2008).
38. Bernstein, M. *et al.* Ewing's sarcoma family of tumors: current management. *Oncologist* **11**, 503-519 (2006).
39. Segal, D. *et al.* In vivo 3D profiling of site-specific human cancer cell morphotypes in zebrafish. *J Cell Biol* **221** (2022).
40. Liu, L. *et al.* Deletion of Cavin/PTRF causes global loss of caveolae, dyslipidemia, and glucose intolerance. *Cell Metab* **8**, 310-317 (2008).
41. Murphey, M.D. *et al.* From the radiologic pathology archives: ewing sarcoma family of tumors: radiologic-pathologic correlation. *Radiographics* **33**, 803-831 (2013).
42. Sheikh, E., Tran, T., Vranic, S., Levy, A. & Bonfil, R.D. Role and significance of c-KIT receptor tyrosine kinase in cancer: A review. *Bosn J Basic Med Sci* **22**, 683-698 (2022).
43. Wang, X., Bove, A.M., Simone, G. & Ma, B. Molecular Bases of VEGFR-2-Mediated Physiological Function and Pathological Role. *Front Cell Dev Biol* **8**, 599281 (2020).

44. Miao, H. *et al*. EphA2 mediates ligand-dependent inhibition and ligand-independent promotion of cell migration and invasion via a reciprocal regulatory loop with Akt. *Cancer Cell* **16**, 9-20 (2009).
45. Dagamajalu, S. *et al*. A pathway map of AXL receptor-mediated signaling network. *J Cell Commun Signal* **15**, 143-148 (2021).
46. Funamoto, S., Meili, R., Lee, S., Parry, L. & Firtel, R.A. Spatial and temporal regulation of 3-phosphoinositides by PI 3-kinase and PTEN mediates chemotaxis. *Cell* **109**, 611-623 (2002).
47. Mazloom-Farsibaf, H., Zou, Q., Hsieh, R., Danuser, G. & Driscoll, M.K. Cellular harmonics for the morphology-invariant analysis of molecular organization at the cell surface. *Nat Comput Sci* **3**, 777-788 (2023).
48. Sohn, J., Lin, H., Fritch, M.R. & Tuan, R.S. Influence of cholesterol/caveolin-1/caveolae homeostasis on membrane properties and substrate adhesion characteristics of adult human mesenchymal stem cells. *Stem Cell Res Ther* **9**, 86 (2018).
49. Kenworthy, A.K. *et al*. Cholera Toxin as a Probe for Membrane Biology. *Toxins (Basel)* **13** (2021).
50. Rocchi, A. *et al*. CD99 inhibits neural differentiation of human Ewing sarcoma cells and thereby contributes to oncogenesis. *J Clin Invest* **120**, 668-680 (2010).
51. Lee, E.J., Lee, H.G., Park, S.H., Choi, E.Y. & Park, S.H. CD99 type II is a determining factor for the differentiation of primitive neuroectodermal cells. *Exp Mol Med* **35**, 438-447 (2003).
52. Singh, V. & Lamaze, C. Membrane tension buffering by caveolae: a role in cancer? *Cancer Metastasis Rev* **39**, 505-517 (2020).
53. Driscoll, M.K. *et al*. Proteolysis-free amoeboid migration of melanoma cells through crowded environments via bleb-driven worrying. *Dev Cell* (2024).
54. Weems, A.D. *et al*. Blebs promote cell survival by assembling oncogenic signalling hubs. *Nature* **615**, 517-525 (2023).
55. Haugh, J.M., Codazzi, F., Teruel, M. & Meyer, T. Spatial sensing in fibroblasts mediated by 3' phosphoinositides. *J Cell Biol* **151**, 1269-1280 (2000).
56. Concordet, J.P. & Haeussler, M. CRISPOR: intuitive guide selection for CRISPR/Cas9 genome editing experiments and screens. *Nucleic Acids Res* **46**, W242-W245 (2018).
57. Lackner, D.H. *et al*. A generic strategy for CRISPR-Cas9-mediated gene tagging. *Nat Commun* **6**, 10237 (2015).
58. Shehwana, H. *et al*. RPPA SPACE: an R package for normalization and quantitation of Reverse-Phase Protein Array data. *Bioinformatics* **38**, 5131-5133 (2022).
59. Akbani, R. *et al*. A pan-cancer proteomic perspective on The Cancer Genome Atlas. *Nat Commun* **5**, 3887 (2014).
60. Siwak, D.R., Li, J., Akbani, R., Liang, H. & Lu, Y. Analytical Platforms 3: Processing Samples via the RPPA Pipeline to Generate Large-Scale Data for Clinical Studies. *Adv Exp Med Biol* **1188**, 113-147 (2019).
61. Jacques, C. *et al*. Murine Models of Bone Sarcomas. *Methods Mol Biol* **1914**, 331-342 (2019).
62. Huisken, J. & Stainier, D.Y. Even fluorescence excitation by multidirectional selective plane illumination microscopy (mSPIM). *Opt Lett* **32**, 2608-2610 (2007).
63. Chen, B. *et al*. Increasing the field-of-view in oblique plane microscopy via optical tiling. *Biomed Opt Express* **13**, 5616-5627 (2022).
64. Driscoll, M.K. *et al*. Robust and automated detection of subcellular morphological motifs in 3D microscopy images. *Nat Methods* **16**, 1037-1044 (2019).

65. Goddard, T.D. *et al*. UCSF ChimeraX: Meeting modern challenges in visualization and analysis. *Protein Sci* **27**, 14-25 (2018).
66. Bankhead, P. *et al*. QuPath: Open source software for digital pathology image analysis. *Sci Rep* **7**, 16878 (2017).
67. Pocock, J. *et al*. TIAToolbox as an end-to-end library for advanced tissue image analytics. *Commun Med (Lond)* **2**, 120 (2022).
68. Marc Macenko , M.N., J. S. Marron, David Borland, John T. Woosley, & Xiaojun Guan , C.S., and Nancy E. Thomas A method for normalizing histology slides for quantitative analysis. *IEEE International Symposium on Biomedical Imaging: From Nano to Macro*, 1107-1110 (2009).
69. Acosta, P.H. *et al*. Intratumoral Resolution of Driver Gene Mutation Heterogeneity in Renal Cancer Using Deep Learning. *Cancer Res* **82**, 2792-2806 (2022).